

Non-perturbative thermal QCD at all temperatures: the case of mesonic screening masses

Mattia Dalla Brida^a, Leonardo Giusti^{b,c}, Tim Harris^d,
Davide Laudicina^{b,c}, and Michele Pepe^c

^a Theoretical Physics Department, CERN,
CH-1211 Geneva 23, Switzerland

^b Dipartimento di Fisica, Università di Milano-Bicocca,
Piazza della Scienza 3, I-20126 Milano, Italy

^c INFN, Sezione di Milano-Bicocca,
Piazza della Scienza 3, I-20126 Milano, Italy

^d School of Physics and Astronomy, University of Edinburgh,
Edinburgh EH9 3JZ, UK

Abstract

We present a general strategy to study non-perturbatively thermal QCD up to very high temperatures. As a first concrete application, we compute the flavour non-singlet meson screening masses at 12 temperatures covering the range from $T \sim 1$ GeV up to ~ 160 GeV in the theory with three massless quarks. The calculation is carried out by Monte Carlo simulations on the lattice by considering large spatial extensions in order to have negligible finite volume effects. For each temperature we have simulated 3 or 4 values of the lattice spacing, so as to perform the continuum limit extrapolation with confidence at a few permille accuracy. Chiral symmetry restoration manifests itself in our results through the degeneracy of the vector and the axial vector channels and of the scalar and the pseudoscalar ones. In the entire range of temperatures explored, the meson screening masses deviate from the free theory result, $2\pi T$, by at most a few percent. These deviations, however, cannot be explained by the known leading term in the QCD coupling constant g up to the highest temperature, where other contributions are still very relevant. In particular the spin-dependent term turns out to be of $O(g^4)$ in the entire range explored, and it remains clearly visible up to the highest temperature, where the pseudoscalar and the vector screening masses are still significantly different within our numerical precision. The intricate pattern of different contributions that we have found explains why it has been difficult in the past to match non-perturbative lattice results at $T \sim 1$ GeV with the analytic behaviour at asymptotically high temperatures.

1 Introduction

Thermal Quantum Chromodynamics (QCD) plays a fundamental rôle in particle and nuclear physics, and in cosmology. Apart from its intrinsic theoretical interest, the collective behaviour of strongly-interacting particles is crucial input for determining the evolution of the Universe in its early stages. Today the quark-gluon plasma is also produced and investigated at heavy-ion colliders, where some of its basic properties are essential to analyze the experimental data.

At asymptotically high temperatures, thermal QCD is described by a three-dimensional effective gauge theory [1,2] which needs to be solved non-perturbatively [3]. As a result, perturbation theory can predict the coefficients of the expansion in the strong coupling constant g only up to a finite order. An important example is the Equation of State (EoS), where non-perturbative contributions start at $O(g^6)$ [4,5]. In the SU(3) Yang–Mills theory, these terms are found to be large up to temperatures two orders of magnitude higher than the critical one [6]. All these facts call for a non-perturbative strategy to study thermal QCD up to very high temperatures, possibly up to the electroweak scale.

The purpose of this paper is to combine information encoded in the three-dimensional effective theory, lattice QCD, step-scaling techniques, and Monte Carlo integration to devise a strategy for studying QCD non-perturbatively up to very high temperatures from first principles. The aim is to generalize to QCD the proposal made in Ref. [6] for the Yang–Mills theory. As a concrete implementation, we consider QCD with $N_f = 3$ flavours of massless quarks in the range of temperatures from about 1 GeV up to approximately 160 GeV¹.

As a first application we compute the non-singlet meson screening masses, maybe the simplest properties of the plasma to be computed. They characterize the exponential decay of two-point correlation functions of fermion bilinears in the spatial directions, i.e. their inverses are the long-distance spatial correlation lengths when mesons are present in the plasma. Screening masses can be easily investigated numerically, they are related to spectral functions, and they signal the restoration of chiral symmetry at high temperature. Their $O(g^2)$ component is known, and is found to be spin independent [7]. The first spin-dependent term is expected to appear only at $O(g^4)$ [8,9]. These masses are therefore ideal quantities to test the strategy proposed in this paper, and to further investigate the relevance of non-perturbative contributions in thermal QCD. It must be said that they have been computed non-perturbatively in lattice QCD for decades, see Ref. [10–13] for recent efforts. These computations, however, are limited to temperatures up to approximately 1 GeV. Here we want to extend the range up to much higher temperatures so as to elucidate the rôle of the various contributions to them.

The paper is organized as follows. In section 2 we review the three-dimensional effective theory, and summarize the properties relevant to this paper. The next section is devoted to introduce the screening masses, and to summarize the known analytic contribution to them. In section 4 we present the strategy for simulating lattice QCD up to very high temperatures. The lattice setup and the raw results are discussed in section 5, while the value of the screening masses in the continuum limit are given in section 6. We discuss and interpret the final results in section 7, while our conclusions and outlook are given in section 8. Notations, conventions, and technical details are reported in several appendices.

¹As the temperature becomes higher and higher, the relevance of the light quark masses becomes quickly negligible.

2 Preliminaries on the effective theory at large T

In thermal QCD at high temperature the physics that takes place at energies much lower than T , or equivalently that involve distances much larger than the temporal direction, can be described by a three-dimensional effective gauge theory [1,2,4], dubbed Electrostatic QCD (EQCD), defined by the action

$$S_{\text{EQCD}} = \frac{1}{g_{\text{E}}^2} \int d^3x \left\{ \frac{1}{2} \text{Tr} [F_{ij} F_{ij}] + \text{Tr} [(D_j A_0)(D_j A_0)] + m_{\text{E}}^2 \text{Tr} [A_0^2] \right\} + \dots \quad (1)$$

where the dots stand for higher dimensional operators, see Ref. [14] for a recent review. The field content is made of the Matsubara zero-modes of the gauge field, while quark fields are decoupled because their modes pick up a mass proportional to πT due to the antiperiodic boundary conditions in the compact direction. The dynamics of the spatial components is governed by a three-dimensional Yang-Mills theory with field strength tensor F_{ij} and dimensionful coupling constant g_{E}^2 . The temporal component of the gauge field A_0 behaves as a three-dimensional scalar field of mass m_{E} which transforms under the adjoint representation of the gauge group. The matching with QCD fixes the low-energy constants to be $m_{\text{E}}^2 = \frac{3}{2} g^2 T^2 + \dots$ and $g_{\text{E}}^2 = g^2 T + \dots$, with g being the renormalized coupling of QCD (usually taken at scale $2\pi T$), and the dots stand for higher order terms in the coupling constant [15].

At asymptotically high T , the coupling g is small and three different energy scales develop so that

$$\frac{g_{\text{E}}^2}{\pi} \ll m_{\text{E}} \ll \pi T. \quad (2)$$

If one is interested in processes at scales of $O(g_{\text{E}}^2)$, the scalar field can be integrated out. The action of the remaining effective theory, dubbed Magnetostatic QCD (MQCD), is given by

$$S_{\text{MQCD}} = \frac{1}{g_{\text{E}}^2} \int d^3x \left\{ \frac{1}{2} \text{Tr} [F_{ij} F_{ij}] \right\} + \dots \quad (3)$$

Being a three-dimensional Yang-Mills theory, it has non-perturbative dynamics and therefore it needs to be solved non-perturbatively [3]. All dimensionful quantities are proportional to the appropriate power of g_{E}^2 times a non-perturbative coefficient.

This in turn implies that, at asymptotically high temperatures, the mass gap developed by thermal QCD is proportional to g_{E}^2 [16]. Finite volume effects are therefore expected to be exponentially small in $g_{\text{E}}^2 L = g^2 T L + \dots$ times a non-perturbative coefficient, see below and appendix C. This fact turns out to be crucial for the strategy outlined in the next sections for studying non-perturbatively thermal QCD up to very high temperatures. At intermediate temperatures, the pre-factors may be relevant in determining what is the mass gap of the theory. But given the relevant scales in the problem, and provided the temperature is sufficiently high with respect to Λ_{QCD} , the mass gap of the theory is always expected to be proportional to the temperature times an appropriate power of the coupling constant [17].

2.1 Fermion correlators

In the effective field theory approach, the quarks are very heavy fields that can be considered, in first approximation, as static external fields. If we choose the non-relativistic representation

of the Dirac γ -matrices and we represent the spinor field as

$$\psi = \begin{pmatrix} \chi \\ \phi \end{pmatrix}, \quad (4)$$

the effective action for the fermion modes can be written as [7–9, 18]

$$S_q^{\text{eff}} = \int d^3x \left\{ i\chi^\dagger \left[M - g_E A_0 + D_3 - \frac{1}{2M} \left(D_k^2 + \frac{g_E}{4i} [\sigma_k, \sigma_l] F_{kl} \right) \right] \chi + \right. \\ \left. i\phi^\dagger \left[M - g_E A_0 - D_3 - \frac{1}{2M} \left(D_k^2 + \frac{g_E}{4i} [\sigma_k, \sigma_l] F_{kl} \right) \right] \phi \right\} + \dots \quad (5)$$

where the mass M is identified with a low-energy constant which, for the lightest modes, is given by $M = \pi T [1 + g^2 / (6\pi^2)] + \dots$

In three dimensions the chiral symmetry group is enlarged with respect to the four-dimensional one due to dimensional reduction. The quark mass M , however, breaks the three-dimensional chiral group down to the unbroken four-dimensional chiral symmetry, and the familiar pattern of chiral symmetry restoration at high temperature is recovered [19]. As we shall see, the restoration of chiral symmetry in thermal QCD will show up in the degeneracy of various masses measured by Monte Carlo simulations at large T .

By scrutinizing the magnitude of the various terms in Eq. (5), the interaction term in the covariant derivatives D_k ($k = 1, 2$) and the spin-dependent contributions proportional to F_{kl} are of higher order in the strong coupling constant with respect to the other terms, and they can be dropped if one is interested in the leading contributions [7]. Before doing so, however, it is interesting to notice that the spin-dependent terms give contributions starting at $O(g^4)$ [8, 9].

3 Definition of the mesonic screening masses

We are interested into the screening masses related to flavour non-singlet fermion bilinear operators

$$\mathcal{O}^a(x) = \bar{\psi}(x) \Gamma_{\mathcal{O}} T^a \psi(x), \quad (6)$$

where $\Gamma_{\mathcal{O}} = \{\mathbb{1}, \gamma_5, \gamma_\mu, \gamma_\mu \gamma_5\}$ characterizes the structure of the operators in the Dirac space, with the latter named as usual as $\mathcal{O} = \{S, P, V_\mu, A_\mu\}$, and we restrict ourselves to $\mu = 2$. Since we will be considering QCD with three massless flavours, the Hermitean matrices T^a are the traceless generators of $SU(3)$ flavour group, and they are normalized so that $\text{Tr}[T^a T^b] = \delta_{ab}/2$. Being singlets in color space, for better readability the summation over the color index is not shown. The spatially separated two-point correlation functions of these operators can be defined as

$$C_{\mathcal{O}}(x_3) = \int dx_0 dx_1 dx_2 \langle \mathcal{O}^a(x) \mathcal{O}^a(0) \rangle, \quad (7)$$

where no summation over a is understood, and the flavour index has been dropped on the l.h.s. since $C_{\mathcal{O}}(x_3)$ does not depend on a when quarks are degenerate. Note that in this case the disconnected Wick contractions do not contribute. The screening masses are defined as

$$m_{\mathcal{O}} = - \lim_{x_3 \rightarrow \infty} \frac{d}{dx_3} \ln [C_{\mathcal{O}}(x_3)], \quad (8)$$

and they characterize the exponential decrease of the correlation function at large spatial distances.

At low temperatures, due to the chiral anomaly and to the spontaneous breaking of chiral symmetry, the masses resulting from the above correlation functions are different. When the temperature is large enough, the vector and axial vector screening masses are expected to become degenerate thanks to the restoration of the non-singlet chiral symmetry. Moreover, at high temperature, the distribution of the topological charge becomes narrower and narrower [20], and only the sector with zero topology contributes de facto to the functional integral [21], see Refs. [20, 22] and references therein for recent results on this topic. This in practice implies a degeneracy of the non-singlet scalar and pseudoscalar screening masses as well.

3.1 Leading interacting contribution in the effective theory

The $O(g^2)$ contribution to the non-singlet mesonic screening masses has been computed in the effective theory [7, 9]. For three massless quarks, the expression reads

$$m_{\mathcal{O}}^{\text{PT}} = 2\pi T + \frac{g_{\text{E}}^2}{3\pi} (1 + 0.93878278) = 2\pi T (1 + 0.032739961 \cdot g^2), \quad (9)$$

where the first two terms come from the low-energy constant M , while the last one is generated by the static potential. Indeed the latter is expected to receive non-perturbative contributions starting only at $O(g^3)$ [7]. In Eq. (9) the masses are independent of the specific mesonic operator \mathcal{O} since, as anticipated, spin-dependent effects are expected to appear at $O(g^4)$.

4 Lattice strategy and setup

In order to set up our strategy for studying thermal QCD non-perturbatively up to very high temperatures, we consider a 4-dimensional lattice with size L_0 in the compact (temporal) direction and extension L along the three spatial directions. As usual, the gauge field is represented by the link variables $U_\mu(x) \in SU(3)$, while the quark and anti-quark fields are given by the flavour multiplets $\psi(x)$ and $\bar{\psi}(x)$ respectively.

4.1 Shifted boundary conditions

The thermal theory is defined by requiring that the fields satisfy shifted boundary conditions in the compact direction [23–25], while we set periodic boundary conditions in the spatial directions. The former consist in shifting the fields by the spatial vector $L_0 \boldsymbol{\xi}$ when crossing the boundary of the compact direction, with the fermions having in addition the usual sign flip. For the gauge fields they read

$$U_\mu(x_0 + L_0, \mathbf{x}) = U_\mu(x_0, \mathbf{x} - L_0 \boldsymbol{\xi}), \quad U_\mu(x_0, \mathbf{x} + \hat{k} L_k) = U_\mu(x_0, \mathbf{x}), \quad (10)$$

while those for the quark and the anti-quark fields are given by

$$\begin{aligned} \psi(x_0 + L_0, \mathbf{x}) &= -\psi(x_0, \mathbf{x} - L_0 \boldsymbol{\xi}), & \psi(x_0, \mathbf{x} + \hat{k} L_k) &= \psi(x_0, \mathbf{x}), \\ \bar{\psi}(x_0 + L_0, \mathbf{x}) &= -\bar{\psi}(x_0, \mathbf{x} - L_0 \boldsymbol{\xi}), & \bar{\psi}(x_0, \mathbf{x} + \hat{k} L_k) &= \bar{\psi}(x_0, \mathbf{x}). \end{aligned} \quad (11)$$

A relativistic thermal field theory in the presence of a shift $\boldsymbol{\xi}$ is equivalent to the very same theory with usual periodic (anti-periodic for fermions) boundary conditions but with a longer extension of the compact direction by a factor $\sqrt{1 + \boldsymbol{\xi}^2}$ [25], i.e. the standard relation between the length and the temperature is modified as $T = 1/(L_0\sqrt{1 + \boldsymbol{\xi}^2})$. Shifted boundary conditions represent a very efficient setup to tackle several problems that are otherwise very challenging both from the theoretical and the numerical viewpoint. A recent example is the EoS of the $SU(3)$ Yang-Mills theory obtained at the permille level up to very high temperatures [6, 26]. The strategy presented in this paper, when supplemented by shifted boundary conditions, paves the way for the computation of the EoS at large temperatures in thermal QCD [27]. Even if the use of shifted boundary conditions is not crucial for the calculation of the screening masses, we have chosen to use them with $\boldsymbol{\xi} = (1, 0, 0)$ so as to share the cost of generating the gauge configurations with that project. The free case computation of the screening masses reported in appendix F, moreover, indicates that the use of shifted boundary conditions with $\boldsymbol{\xi} = (1, 0, 0)$ makes discretization effects in the screening masses milder.

4.2 Renormalization and lines of constant physics

A hadronic scheme is not a convenient choice to renormalize QCD non-perturbatively when considering a broad range of temperatures spanning several orders of magnitude. In fact, this would require to accommodate on a single lattice the temperature and the hadronic scale which may differ by orders of magnitude, making the numerical computations prohibitive. A similar problem is encountered when renormalizing QCD non-perturbatively, and it was solved many years ago by introducing a step-scaling technique [28, 29].

In order to solve our problem, we build on that knowledge by considering a non-perturbative definition of the coupling constant, $\bar{g}_{\text{SF}}^2(\mu)$, which can be computed precisely on the lattice for values of the renormalization scale μ which span several orders of magnitude. Making a definite choice, in this section we use the definition based on the Schrödinger functional (SF) [30], but other choices are available today. In particular later on in the paper we will also consider the gradient flow (GF) definition [31–33]. Once $\bar{g}_{\text{SF}}^2(\mu)$ is known in the continuum limit for $\mu \sim T$ [32, 34], we renormalize thermal QCD by fixing the value of the renormalized coupling constant at fixed lattice spacing a to be

$$\bar{g}_{\text{SF}}^2(g_0^2, a\mu) = \bar{g}_{\text{SF}}^2(\mu), \quad a\mu \ll 1. \quad (12)$$

This is the condition that fixes the so-called lines of constant physics, i.e. the dependence of the bare coupling constant g_0^2 on the lattice spacing, for values of a at which the scale μ and therefore the temperature T can be easily accommodated. QCD at temperature T can then be simulated at different values of the lattice spacings, and the continuum limit of the observable of interest can be taken with confidence. All the technical details on how this procedure is implemented in practice are given in appendix B.

4.3 Lattice setup

We perform our study at the 12 values of the temperature, T_0, \dots, T_{11} , reported in Table 1, covering the range from approximately 1 GeV up to about 160 GeV. For the 9 highest ones, T_0, \dots, T_8 , gluons are regularized with the Wilson plaquette action in Eq. (20) of appendix A, while for the 3 lowest temperatures, T_9, T_{10} and T_{11} , we adopt the tree-level improved gauge action in Eq. (22). The three massless flavours are always discretized by the $O(a)$ -improved

Wilson–Dirac operator defined in appendix A. In order to extrapolate the results to the continuum limit, several lattice spacings are simulated at each temperature with the extension of the fourth dimension being $L_0/a = 4, 6, 8$ or 10 . The bare coupling and the critical mass m_{cr} are fixed at each lattice spacing from the results of Refs. [32–35] by adopting the strategy outlined above and explained in details in appendix B.

4.4 Finite-volume effects

As we have discussed in section 2, at high temperature the mass gap of the theory is proportional to T times an appropriate power of the coupling constant. As a consequence, finite-size effects are proportional to LT times a coefficient that tends to decrease logarithmically with the temperature, see Refs. [25, 36] and appendix C. For this reason, the lattices that we consider have rather large spatial directions, i.e. $L/a = 288$, so that LT ranges always from 20 to 50. We profit here from the continuous theoretical and algorithmic progress in the simulation of gauge theories, as well as the steady progress in HPC hardware, which has made it possible to simulate lattices with a very large number of points. As we will discuss below, we also always explicitly check that finite-size effects are negligible within the statistical precision of our observables.

4.5 Restricting to the zero-topological sector

At high temperature, the topological charge distribution is expected to be highly peaked at zero. In particular, in QCD with three light degenerate flavours of mass m , the instanton analysis predicts the topological susceptibility to be proportional to $T^{-b}m^3$ with $b \sim 8$. The analogous prediction for the Yang–Mills theory has been verified explicitly on the lattice [20]. When fermions are introduced, the numerical computations become significantly more involved and the systematics are still difficult to control. The simulations done so far, however, are compatible with the T -dependence predicted by the semi-classical analysis [37, 38]. As a result, already at the lower end of the temperature range considered here, $T = 1$ GeV, the probability to encounter a configuration with non-zero topology in our volumes is expected to be several orders of magnitude smaller than the permille or so. This is even less probable in the limit of massless quarks. We can therefore restrict our calculations to the sector with zero topology, and generate the ensembles of gauge field configurations by a Hybrid Monte Carlo (HMC) as described in Appendix E.

5 Lattice correlation functions and screening masses

After integrating over the fermion fields, the lattice version of the correlation function in Eq. (7) reads

$$C_{\mathcal{O}}(x_3 - y_3) = -\frac{a^3}{2} \sum_{x_0, x_1, x_2} \langle \text{Tr} \left[\Gamma_{\mathcal{O}} D^{-1}(x, y) \Gamma_{\mathcal{O}} \gamma_5 D^{\dagger-1}(x, y) \gamma_5 \right] \rangle, \quad (13)$$

where Tr indicates the trace over the color and spin indices, and the same name as in the continuum is used since the ambiguity can be resolved from the context. The quark propagator $D^{-1}(x, y)$ from the source point y to the sink x is the inverse of the $O(a)$ -improved Wilson–Dirac operator defined in Eq. (25) computed at the critical value of the quark mass. At

high temperature, the inversion of the lattice Dirac operator needs to be done with particular care. This is because the lowest Matsubara frequency πT provides an infrared cutoff to quark propagation and, as a result, the matrix elements of $D^{-1}(x, y)$ become extremely small when $T|x - y| \gg 1$. At those distances a very accurate solution of the Dirac equation is required, and the brute-force approach of simply implementing higher-precision by requiring a smaller tolerance is not practicable. We have solved this problem by introducing a distance preconditioning of the Dirac equation as discussed in Appendix D.

The two-point correlation functions for the scalar and pseudoscalar densities and for the vector and axial currents have been computed on all lattices generated, see Tables 4 and 7. We report in Tables 8 and 9 the number of Molecular Dynamics Units (MDUs) after the thermalization phase of each HMC chain, the number of MDUs skipped between two consecutive independent configurations, and the number of local sources per configuration on which the Wilson–Dirac operator has been inverted. The best estimates of $C_{\mathcal{O}}(x_3)$ on each configuration have been obtained by properly averaging their values from all local sources and then symmetrizing the correlators with respect to $x_3 = L/2$. We carefully monitored the autocorrelation of the correlators, and we never observed long autocorrelation times with respect to the number of MDUs skipped between two consecutive measurements.

Within our statistical errors, we observe an excellent agreement between the scalar and pseudoscalar correlators as well as between the vector and axial ones at intermediate and large distances. This is a distinctive feature of the restoration of chiral symmetry which occurs at high temperatures. For this reason, in the rest of the paper we focus our discussion on the pseudoscalar and the vector correlators only.

Once the correlation functions in Eq. (13) have been computed, effective screening masses are defined as

$$m_{\mathcal{O}}(x_3) = \frac{1}{a} \operatorname{arcosh} \left[\frac{C_{\mathcal{O}}(x_3 + a) + C_{\mathcal{O}}(x_3 - a)}{2C_{\mathcal{O}}(x_3)} \right]. \quad (14)$$

Their values for the pseudoscalar density (left panel) and the vector current (right panel) are shown in Fig. 1 for T_3 and $L_0/a = 6$. An analogous behaviour is observed for all other lattices. We obtain very long plateaux thanks to the fact that we have simulated lattices with a very large spatial extension, and that there is no signal-to-noise ratio problem at high temperature. To determine the best estimates of the screening masses $m_{\mathcal{O}}$, we start by fitting the symmetrized correlator to a sum of two exponentials from a minimum value of x_3/a up to the last point available. The minimum value is chosen so as to obtain a good quality of the two-exponential fit, and at the same time a statistically non-zero contribution from the sub-leading exponential. From the result of this fit we then estimate the minimum value x_3^{\min}/a from which the contamination in the effective mass due to the second exponential is negligible with respect to the statistical precision that we obtain by fitting the effective mass to a constant from x_3^{\min}/a up to the last available point. We then verify explicitly that a constant value fits well the effective mass from x_3^{\min}/a up to the end of the plateau, and that by increasing x_3^{\min}/a by a few units the result of the fit does not change significantly. Examples of results of these fits are represented in Fig. 1 as straight lines again for T_3 and $L_0/a = 6$. Our best estimates of the screening masses are reported in Tables 8 and 9 for all the lattices simulated. The statistical error is at most a few permille in all cases. In order to profit from the correlations in our data for reducing the statistical errors, we also compute $(m_V - m_P)/(2\pi T)$ and report its values in Tables 8 and 9 as well. This combination is particularly interesting because it is a measure of the spin-dependent terms which can be computed very precisely.

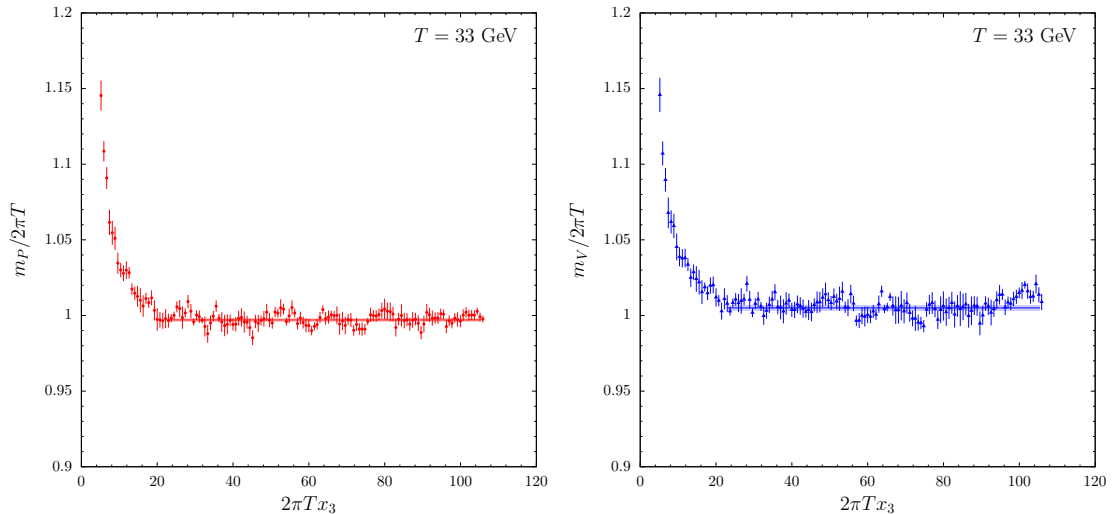


Figure 1: Plot of the effective masses, normalized to $2\pi T$, for the pseudoscalar (left) and vector (right) correlators at the temperature T_3 for $L_0/a = 6$.

We have explicitly checked that finite volume effects are negligible within our statistical errors: we have generated three more lattices at the highest and at the lowest temperatures for the smallest spatial volumes corresponding to $L_0/a = 6$, $L_0/a = 10$, and $L_0/a = 8$ for T_0 , T_1 , and T_{11} respectively. These lattices have the same dimensions in the compact and in the x_3 directions as those in Tables 4 and 7 but smaller extension in the other two spatial directions. The screening masses computed on them are in agreement with those calculated on the larger volume, see appendix E for the details, and therefore we can safely assume that our results have negligible finite-volume effects within the statistical precision.

6 Continuum limit of meson screening masses

The results that we have collected at finite lattice spacing have to be extrapolated to the continuum limit along lines of constant physics. For $O(a)$ -improved actions, the Symanzik effective theory predicts the leading behaviour of the lattice artifacts to be of order a^2 . We can accelerate the convergence to the continuum by introducing the tree-level improved definitions

$$m_{\mathcal{O}} \longrightarrow m_{\mathcal{O}} - \left[m_{\mathcal{O}}^{\text{free}} - 2\pi T \right], \quad (15)$$

where $m_{\mathcal{O}}^{\text{free}}$ is the mass in the free lattice theory. As shown in the appendix F, where the computation is reported, the latter is the same for all non-singlet meson masses. From now on we will consider always the tree-level improved definition of the screening masses and indicate them with $m_{\mathcal{O}}$.

All data for the improved pseudoscalar (left panel) and vector (right panel) screening masses are represented in Fig. 2 where, in order to improve the readability, data corresponding to T_i ($i = 0, \dots, 11$) are shifted downward by $0.02 \times i$. The analogous plot for $(m_V - m_P)$ is shown in Fig. 3. At each temperature, lattice artifacts are well described by a single correction

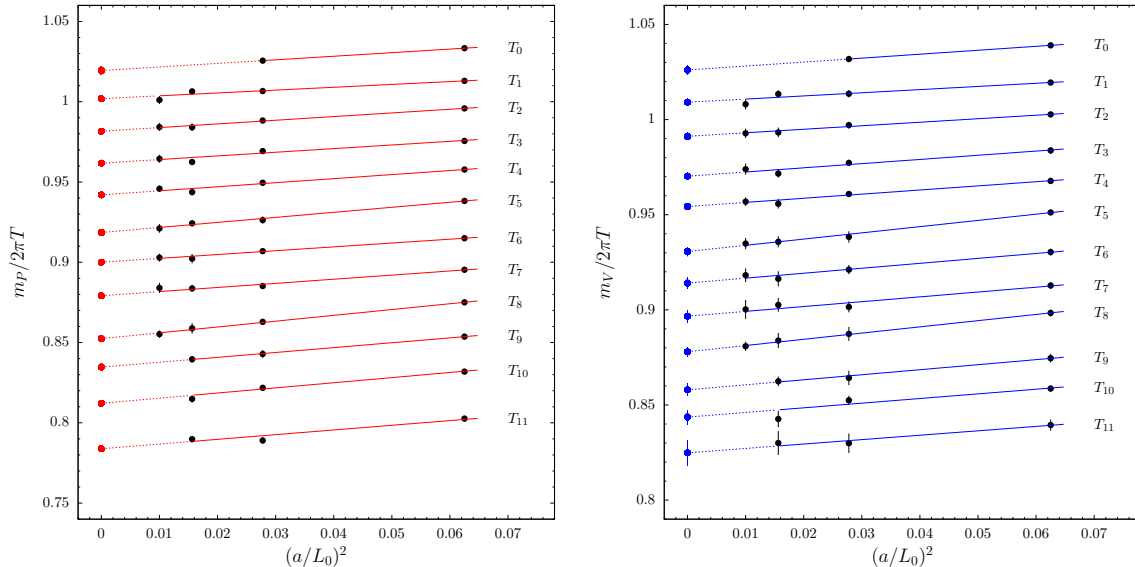


Figure 2: Numerical results for the tree-level improved pseudoscalar (left panel) and vector (right panel) screening masses at finite lattice spacing (black dots). The lines in the panels represent the linear extrapolations in $(a/L_0)^2$ to the continuum limit. Each temperature is analyzed independently from the others. Data corresponding to T_i ($i = 0, \dots, 11$) are shifted downward by $0.02 \times i$ for better readability.

proportional to $(a/L_0)^2$. Indeed by fitting each data set linearly in $(a/L_0)^2$, the values of χ^2/dof are all around 1 with just a few outliers which, however, are not surprising given the large amount of data and fits. The results of the fits are shown in the plots of Figs. 2 and 3 as straight lines. For the mass difference, the coefficient of $(a/L_0)^2$ is found to be compatible with zero at all temperatures. We take the continuum limit values from these fits as our best results for the non-singlet meson screening masses and their difference. They are reported in Table 1 for all the 12 temperatures considered. As a further check of the extrapolations, we have fitted the data by excluding the coarsest lattice spacing, i.e. $L_0/a = 4$, for the temperatures T_1, \dots, T_8 for which we have 4 data points. The intercepts are in excellent agreement with those of the previous fits, albeit with a slightly larger error. For the same sets of data, we have also attempted to include in the fit a $(a/L_0)^2 \ln(a/L_0)$ or a $(a/L_0)^4$ term. The resulting coefficients are compatible with zero. Given the high quality of the fits and of

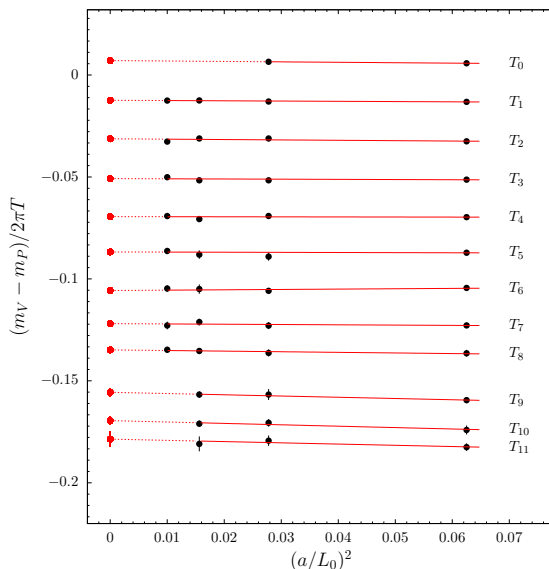


Figure 3: As in Fig. 2 but for the mass difference.

the data, it is not necessary to model the temperature dependence of the discretization effects so as to perform a global fit of the data.

T	$T(\text{GeV})$	$\frac{m_P}{2\pi T}$	$\frac{m_V}{2\pi T}$	$\frac{(m_V - m_P)}{2\pi T}$
T_0	164.6(5.6)	1.0194(25)	1.0261(23)	0.0071(7)
T_1	82.3(2.8)	1.0219(15)	1.0291(18)	0.0076(4)
T_2	51.4(1.7)	1.0216(16)	1.0312(18)	0.0087(4)
T_3	32.8(1.0)	1.0217(15)	1.0302(19)	0.0092(6)
T_4	20.63(63)	1.0220(15)	1.0343(17)	0.0105(6)
T_5	12.77(37)	1.0185(18)	1.0306(24)	0.0132(10)
T_6	8.03(22)	1.0200(18)	1.0341(28)	0.0143(13)
T_7	4.91(13)	1.0192(18)	1.037(3)	0.0181(14)
T_8	3.040(78)	1.0124(18)	1.0380(25)	0.0252(13)
T_9	2.833(68)	1.0147(24)	1.038(3)	0.0244(20)
T_{10}	1.821(39)	1.0122(18)	1.044(4)	0.0305(20)
T_{11}	1.167(23)	1.0039(20)	1.045(6)	0.041(4)

Table 1: Best results for the pseudoscalar, m_P , and the vector, m_V , non-singlet screening masses in the continuum limit together with their difference.

7 Discussion and interpretation of the results

The main results of this paper are the non-singlet meson screening masses reported in Table 1. They have been computed in a wide temperature range starting from $T \sim 1$ GeV up to 160 GeV or so with a precision of a few permille.

The first observation is that, as anticipated in section 5, within our rather small statistical errors we find an excellent agreement between the scalar and pseudoscalar masses and the vector and axial ones. This is a clear manifestation of the restoration of chiral symmetry occurring at high temperature. For this reason we do not show explicitly the results for the other two channels, and we focus on the pseudoscalar and vector masses.

A second observation is that the bulk of the non-singlet meson screening masses is given by the free-theory value, $2\pi T$, plus a few percent positive contribution over the entire range of temperatures explored.

Thanks to the precision of our results, we can scrutinize in detail the temperature dependence induced by the non-trivial dynamics. We introduce the function $\hat{g}^2(T)$ defined as

$$\frac{1}{\hat{g}^2(T)} \equiv \frac{9}{8\pi^2} \ln \frac{2\pi T}{\Lambda_{\overline{\text{MS}}}} + \frac{4}{9\pi^2} \ln \left(2 \ln \frac{2\pi T}{\Lambda_{\overline{\text{MS}}}} \right), \quad (16)$$

where $\Lambda_{\overline{\text{MS}}} = 341$ MeV is taken from Ref. [39]. It corresponds to the 2-loop definition of the strong coupling constant in the $\overline{\text{MS}}$ scheme at the renormalization scale $\mu = 2\pi T$. For our purposes, however, this is just a function of the temperature T , suggested by the effective theory analysis, that we use to analyze our results².

²One could also use a non-perturbative definition of the coupling constant, such as \bar{g}_{SF}^2 . In this case, however, comparing our data with the analytic results in the literature would be more involved.

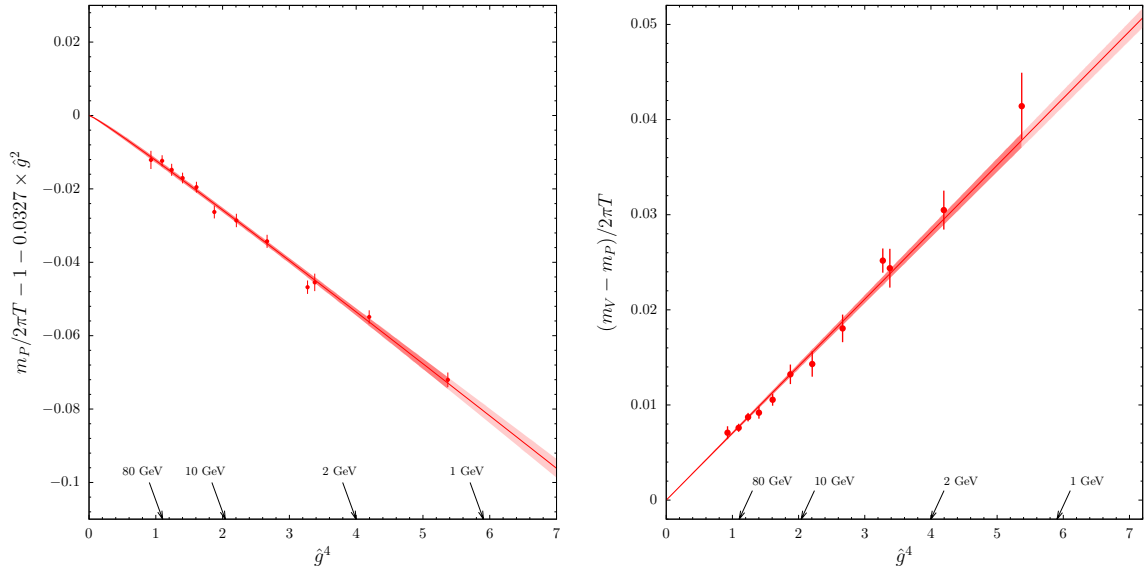


Figure 4: Left: the pseudoscalar mass, normalized to $2\pi T$, subtracted of the analytically known contributions versus \hat{g}^4 . Right: the vector-pseudoscalar mass difference, normalized to $2\pi T$, versus \hat{g}^4 . Red bands represent the best fits of the data as explained in the text.

7.1 Pseudoscalar mass

We start our analysis by fitting the pseudoscalar mass in the third column of Table 1 to a quartic polynomial in \hat{g} . The intercept turns out to be compatible with 1, as predicted by the free theory, within a large error. We have thus enforced it to the free-theory value, $p_0 = 1$, and we have fitted again the data. The coefficient of the \hat{g}^2 term turns out to be compatible with the theoretical expectation in Eq. (9) within again a large uncertainty. We have thus fixed also this coefficient to its analytical value, $p_2 = 0.032739961$, and we have performed again the quartic fit of the form

$$\frac{m_P}{2\pi T} = p_0 + p_2 \hat{g}^2 + p_3 \hat{g}^3 + p_4 \hat{g}^4. \quad (17)$$

As a result, for the fit parameters we obtain $p_3 = 0.0038(22)$, $p_4 = -0.0161(17)$ and $\text{cov}(p_3, p_4)/[\sigma(p_3)\sigma(p_4)] = -1.0$ with the excellent value of $\chi^2/\text{dof} = 0.75$. The quality of the fit can be appreciated in the left plot of Fig. 4, where $m_P/(2\pi T)$ - subtracted of the analytically known contributions - is shown as a function of \hat{g}^4 together with the best fit to Eq. (17). If the cubic coefficient is enforced to vanish, i.e. $p_3 = 0$, the fit returns $p_4 = -0.01323(20)$ with again an excellent value of $\chi^2/\text{dof} = 0.96$. It is clear that the subtracted data lie on a straight line over two orders of magnitude in the temperature, or equivalently over a factor almost 6 in \hat{g}^4 . The polynomial in Eq. (17) is indeed the best parameterization of our results over the entire range of temperatures explored.

The quartic term is necessary to explain the data over the entire temperature range. In particular at the electroweak scale or so, it is still approximately half of the total contribution due to the interactions. It is interesting to notice that the sign of the quartic term is negative, opposite to the one of the quadratic contribution. The magnitude turns out to be

approximately 2–3 times smaller than p_2 . When the data are plotted as a function of \hat{g}^2 , the quartic contribution competes with the quadratic one to bend down the pseudoscalar mass as shown in Fig. 5. Toward the lower end of the range, the competition between this term and the leading one results in an effective slope of opposite sign with respect to the analytically known one. At $T \sim 1$ GeV, the various terms cancel each other and the mass turns out to be very close to free-value $2\pi T$.

7.2 Vector mass

The mass difference $(m_V - m_P)/(2\pi T)$ is an interesting quantity to investigate the magnitude of the spin-dependent contributions. We plot our results for this quantity (last column of Table 1) as a function of \hat{g}^4 on the right panel of Fig. 4. The data turn out to lie on a straight line with a vanishing intercept. By fitting them to

$$\frac{(m_V - m_P)}{2\pi T} = s_4 \hat{g}^4, \quad (18)$$

we obtain $s_4 = 0.00704(14)$ with $\chi^2/\text{dof} = 0.79$. It is remarkable that the spin-dependent contribution can be parameterized by a single $O(\hat{g}^4)$ term in the entire range of temperatures explored. Furthermore, it remains clearly visible up to the highest temperature, where the pseudoscalar and the vector masses are still significantly different within our numerical precision, see Fig. 5. The best polynomial that parameterizes our results for the vector mass (fourth column of Table 1) is therefore

$$\frac{m_V}{2\pi T} = p_0 + p_2 \hat{g}^2 + p_3 \hat{g}^3 + (p_4 + s_4) \hat{g}^4, \quad (19)$$

where p_0, \dots, p_4 are those in Eq. (17) while s_4 is taken from Eq. (18). The covariances of the coefficients p_3 and p_4 with s_4 are $\text{cov}(p_3, s_4)/[\sigma(p_3)\sigma(s_4)] = 0.08$ and $\text{cov}(p_4, s_4)/[\sigma(p_4)\sigma(s_4)] = -0.07$.

As shown in Fig. 5, the quartic contribution is necessary to explain the data over the entire temperature range. In particular at the electroweak scale, it is still approximately 15% of the total contribution due to the interactions. Also for the vector mass, the coefficient of the quartic term in Eq. (19) has an opposite sign with respect to p_2 , but it is approximately half of the analogous one for the pseudoscalar. When the mass is plotted as a function of \hat{g}^2 , see Fig. 5, the quartic contribution competes with the quadratic one but is not large enough to push down the vector mass, at least in the range considered. At the lower end of our range, $T \sim 1$ GeV, it is the spin-dependent term that is responsible for the deviation of the vector mass from $2\pi T$, given the cancellation among the other terms.

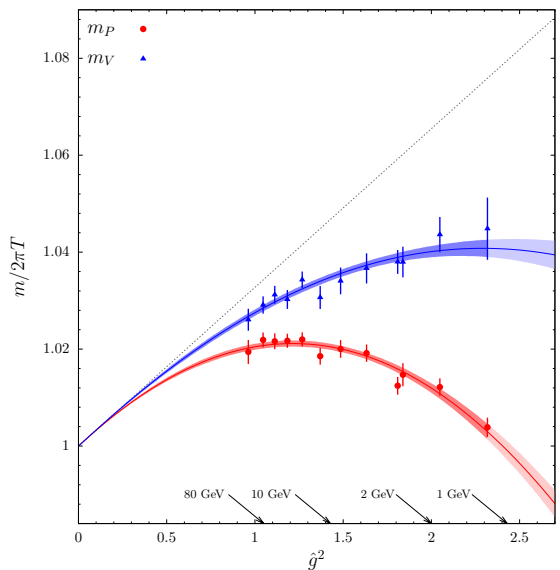


Figure 5: Pseudoscalar (red) and vector (blue) screening masses versus \hat{g}^2 . The bands represent the best fits in Eqs. (17) and (19), while the dashed line is the analytically known contribution.

In the literature, non-perturbative computations of these masses are available only up to temperatures of 1 GeV or so [12]. Even if these results have been obtained at the physical values of the quark masses or close by, they are in agreement with ours at those temperatures within the rather large errors. In fact, the relevance of the quark masses at that temperature is very mild, and it becomes quickly negligible as the temperature increases. The intricate pattern of different contributions that we have just discussed, however, explains why it has been difficult in the past to match non-perturbative lattice results at $T \lesssim 1$ GeV with the expected analytic behaviour at asymptotically high temperatures. Indeed the apparently small 2-4% effect in the screening masses induced by the interactions among quarks and gluons encodes a lot of interesting non-trivial information about the dynamics of the plasma. When the corresponding non-perturbative computations in the three-dimensional effective theory will become available, the matching with the results presented here will allow to shed light on the origin of the various terms, and to verify non-perturbatively the effective theory paradigm over several orders of magnitude in the temperature.

8 Conclusions and outlook

The continuous theoretical and algorithmic progress in the simulation of gauge theories, as well as the steady progress in HPC hardware, has made it possible to simulate lattices with a very large number of points. This has opened to the possibility of studying thermal gauge theories non-perturbatively at very high temperature. Here we have profited from this progress to simulate, for the first time, QCD with three massless flavours at temperatures ranging from 1 GeV up to the electroweak scale and above. We have renormalized the theory by imposing the value of the strong coupling constant defined non-perturbatively in a finite-volume renormalization scheme. The entire strategy has been implemented by discretizing fermions with the $O(a)$ -improved Wilson–Dirac operator. This is a theoretically-sound regularization, not only simple to simulate, but which enjoys de-facto automatic $O(a)$ -improvement at high temperature [27].

In the very high temperature regime, the non-singlet meson screening masses are perhaps the simplest computations to start with. For QCD with three massless flavours, we observe an excellent agreement within our statistical errors between the scalar and pseudoscalar masses as well as between the vector and axial ones. This is a clear manifestation of the restoration of chiral symmetry for temperatures from $T \sim 1$ GeV up to 160 GeV. Our best results for the pseudoscalar and vector masses are reported in Table 1, they are parameterized in Eqs. (17) and (19), and they are shown in Fig. 5. In the entire range explored, the meson screening masses deviate from the free theory result, $2\pi T$, by at most a few percent. These deviations, however, cannot be explained by the known leading term in the coupling constant up to the highest temperature, where other contributions are still very significant. The latter bend down the pseudoscalar mass to the point that the effective slope in \hat{g}^2 , at the lower temperatures, is of opposite sign with respect to the analytically known one. The spin-dependent contributions are very well parameterized, within our statistical errors, by a single $O(\hat{g}^4)$ term in the entire range of temperature explored. At low temperatures, and in particular at $T \sim 1$ GeV, this term is responsible for the deviation of the vector mass from $2\pi T$. It remains clearly visible up to the highest temperature, where the pseudoscalar and the vector masses are still significantly different within our numerical precision.

The intricate pattern of different contributions that we have found explains why it has been difficult in the past to match non-perturbative lattice results at $T \lesssim 1$ GeV with the known analytic behaviour at asymptotically high temperatures. From a more theoretical point of view, when the corresponding non-perturbative computations in the three-dimensional effective theory will become available, the matching with the results presented here will allow to shed light on the origin of the various terms, and to verify non-perturbatively the effective theory paradigm. At the same time, the possibility of studying QCD at high temperatures by Monte Carlo simulations, makes the perturbative results less compelling especially if higher and higher orders must be taken into account.

The strategy proposed here clears the way to compute many other interesting properties of thermal QCD in the high temperature regime. Indeed this work is part of a larger effort which aims at computing the EoS non-perturbatively up to the electroweak scale or so.

Acknowledgement

We wish to thank Mikko Laine for correspondence on the strong coupling expansion of the screening masses. We acknowledge PRACE for awarding us access to the HPC system MareNostrum4 at the Barcelona Supercomputing Center (Proposals n. 2018194651 and 2021240051) where most of the numerical results presented in this paper have been produced. We also thanks CINECA for providing us with computer-time on Marconi (CINECA- INFN, CINECA-Bicocca agreements, ISCRA B projects HP10BF2OQT and HP10B1TWRR). The R&D has been carried out on the PC clusters Wilson and Knuth at Milano-Bicocca. We thank all these institutions for the technical support. Finally we acknowledge partial support by the INFN project ‘‘High performance data network’’. T. H. has been supported by UK STFC CG ST/P000630/1.

A Lattice actions

The QCD lattice action is $S = S_G + S_F$ where S_G and S_F are the pure gauge and the fermionic parts respectively. In this paper we use both the Wilson plaquette action, $S_G^{(W)}$, and the tree-level Symanzik improved action, $S_G^{(I)}$, for the pure gauge sector. The former is defined as [40]

$$S_G^{(W)} = \frac{1}{g_0^2} \sum_x \sum_{\mu, \nu} \text{Re Tr} [\mathbb{1} - U_{\mu\nu}(x)] \quad (20)$$

where the plaquette field is

$$U_{\mu\nu}(x) = U_\mu(x) U_\nu(x + a\hat{\mu}) U_\mu^\dagger(x + a\hat{\nu}) U_\nu^\dagger(x), \quad (21)$$

and $\hat{\mu}, \hat{\nu}$ are unit vectors oriented along the directions μ, ν respectively. The tree-level Symanzik improved action is defined as [41]

$$S_G^{(I)} = \frac{1}{g_0^2} \sum_x \sum_{\mu, \nu} \text{Re} \left\{ \frac{5}{3} \text{Tr} [\mathbb{1} - U_{\mu\nu}(x)] - \frac{1}{12} \text{Tr} [\mathbb{1} - \tilde{U}_{\mu\nu}(x)] \right\} \quad (22)$$

where $\tilde{U}_{\mu\nu}$ is a rectangular two-plaquette field defined as

$$\tilde{U}_{\mu\nu}(x) = U_\mu(x) U_\mu(x + a\hat{\mu}) U_\nu(x + 2a\hat{\mu}) U_\mu^\dagger(x + a\hat{\mu} + a\hat{\nu}) U_\nu^\dagger(x + a\hat{\nu}) U_\nu^\dagger(x). \quad (23)$$

The fermionic part of the action is

$$S_F = a^4 \sum_x \bar{\psi}(x)(D + M_0)\psi(x) \quad (24)$$

where M_0 is the bare quark mass matrix and D is the lattice Dirac operator for which we consider the $O(a)$ -improved definition [42, 43]

$$D = D_w + aD_{sw} . \quad (25)$$

The first term D_w is the massless Wilson-Dirac operator given by

$$D_w = \frac{1}{2} \{ \gamma_\mu (\nabla_\mu^* + \nabla_\mu) - a \nabla_\mu^* \nabla_\mu \} , \quad (26)$$

where ∇_μ^*, ∇_μ are covariant lattice derivatives that act on the quark fields as follows

$$\begin{aligned} a \nabla_\mu \psi(x) &= U_\mu(x) \psi(x + a\hat{\mu}) - \psi(x) , \\ a \nabla_\mu^* \psi(x) &= \psi(x) - U_\mu^\dagger(x - a\hat{\mu}) \psi(x - a\hat{\mu}) . \end{aligned} \quad (27)$$

The second term D_{sw} is the Sheikholeslami-Wohlert operator

$$D_{sw} \psi(x) = c_{sw}(g_0) \frac{1}{4} \sigma_{\mu\nu} \widehat{F}_{\mu\nu}(x) \psi(x) \quad (28)$$

where $\sigma_{\mu\nu} = \frac{i}{2} [\gamma_\mu, \gamma_\nu]$. The field $\widehat{F}_{\mu\nu}(x)$ is the clover discretization of the field strength tensor which is given by

$$\widehat{F}_{\mu\nu}(x) = \frac{i}{8a^2} \{ Q_{\mu\nu}(x) - Q_{\nu\mu}(x) \} , \quad (29)$$

with

$$\begin{aligned} Q_{\mu\nu}(x) &= U_\mu(x) U_\nu(x + a\hat{\mu}) U_\mu^\dagger(x + a\hat{\nu}) U_\nu^\dagger(x) \\ &+ U_\nu(x) U_\mu^\dagger(x - a\hat{\mu} + a\hat{\nu}) U_\nu^\dagger(x - a\hat{\mu}) U_\mu(x - a\hat{\mu}) \\ &+ U_\mu^\dagger(x - a\hat{\mu}) U_\nu^\dagger(x - a\hat{\mu} - a\hat{\nu}) U_\mu(x - a\hat{\mu} - a\hat{\nu}) U_\nu(x - a\hat{\nu}) \\ &+ U_\nu^\dagger(x - a\hat{\nu}) U_\mu(x - a\hat{\nu}) U_\nu(x + a\hat{\mu} - a\hat{\nu}) U_\mu^\dagger(x) . \end{aligned} \quad (30)$$

By a proper non-perturbative tuning of the coefficient $c_{sw}(g_0)$, all $O(a)$ discretization effects generated by the action in on-shell correlation functions can be removed [43, 44]. For the Wilson plaquette action this is achieved by fixing $c_{sw}(g_0)$ to [45]

$$c_{sw}^{(W)}(g_0) = \frac{1 - 0.194785 g_0^2 - 0.110781 g_0^4 - 0.0230239 g_0^6 + 0.137401 g_0^8}{1 - 0.460685 g_0^2} , \quad (31)$$

while for the tree-level Symanzik improved gauge action the analogous expression is [46]

$$c_{sw}^{(I)}(g_0) = \frac{1 - 0.1921 g_0^2 - 0.1378 g_0^4 + 0.0717 g_0^6}{1 - 0.3881 g_0^2} . \quad (32)$$

T	$\bar{g}_{\text{SF}}^2(\mu = T\sqrt{2})$	T (GeV)
T_0	–	164.6(5.6)
T_1	1.11000	82.3(2.8)
T_2	1.18446	51.4(1.7)
T_3	1.26569	32.8(1.0)
T_4	1.3627	20.63(63)
T_5	1.4808	12.77(37)
T_6	1.6173	8.03(22)
T_7	1.7943	4.91(13)
T_8	2.0120	3.040(78)

Table 2: Values of the SF couplings corresponding to the lines of constant physical temperature that we consider.

B Temperature values and lines of constant physics

In this appendix we discuss in detail how the 12 temperatures T_0, \dots, T_{11} have been chosen, and how for each temperature the various lattice spacings and the corresponding bare parameters have been fixed so as to define lines of constant physics.

Either for quarks or gluons we remind that shifted boundary conditions, always with $\xi = (1, 0, 0)$, have been enforced in the compact direction so that $T = 1/(\sqrt{2}L_0)$. The temperature values T_0, \dots, T_8 and T_9, \dots, T_{11} have then been fixed by specifying the values of the Schrödinger functional (SF) and the gradient flow (GF) finite-volume couplings respectively by using the results of Refs. [32–35].

B.1 High temperatures

The temperature values T_0, \dots, T_8 are fixed from the results in Refs. [32, 34, 35] by imposing the relation

$$T = \frac{1}{L_0\sqrt{2}} = \frac{\mu}{\sqrt{2}}, \quad (33)$$

where μ is the renormalization scale of the Schrödinger functional (SF) coupling $\bar{g}_{\text{SF}}^2(\mu)$ determined in a box with linear extension $L_0^{\text{SF}} = 1/\mu$ and SF boundary conditions enforced, i.e. $L_0 = L_0^{\text{SF}}$. From Ref. [39] we obtain

$$\bar{g}_{\text{SF}}^2(\mu_0) = 2.0120 \quad \Rightarrow \quad \mu_0 = 4.30(11) \text{ GeV} = T_8\sqrt{2}, \quad (34)$$

where the contribution from the charm and bottom quarks can be safely neglected given the current level of precision on the combination of the pion and kaon decay constants used to fix the overall scale [47], see Ref. [48] for more details. Given T_8 , the higher values of the temperature can be inferred through the relation

$$\ln\left(\frac{\mu}{\mu_0}\right) = \int_{\bar{g}_{\text{SF}}(\mu_0)}^{\bar{g}_{\text{SF}}(\mu)} \frac{dg}{\beta_{\text{SF}}(g)}, \quad (35)$$

which readily follows from integrating the definition of the β -function. By using the results of Ref. [34], the non-perturbative β -function of the SF coupling can be parameterized over the range of couplings of interest as (cf. Eq. (2.34) of Ref. [35])

$$\beta_{\text{SF}}(\bar{g}) = -\bar{g}^3 \sum_{n=0}^3 b_n \bar{g}^{2n}, \quad \bar{g}^2 \in [0, 2.45], \quad (36)$$

with b_0, b_1, b_2 being the perturbative coefficients of the SF β -function (for $N_f = 3$)

$$(4\pi)b_0 = \frac{9}{4\pi}, \quad (4\pi)^2 b_1 = \frac{4}{\pi^2}, \quad (4\pi)^3 b_2 = -0.064(27),$$

while b_3 is an effective higher-order contribution extracted from the non-perturbative data

$$(4\pi)^4 b_3^{\text{eff}} = 4(3). \quad (37)$$

Given this representation, we integrated Eq. (35) numerically using the result for μ_0 in Eq. (34), and we obtained the values for the temperatures reported in Table 2.

L_0/a	$\delta am_{\text{cr}}^{(0)}$	$\delta am_{\text{cr}}^{(1)}$
4	-0.0015131	0.0120930
6	-0.0006384	0.0008250
8	-0.0003209	0.0001878
10	-0.0001835	0.0000751
12	-0.0001145	0.0000403
16	-0.0000531	0.0000168

Table 3: Tree-level and one-loop cutoff effects for the critical mass in the SF for setup A with background gauge field, $\theta = \pi/5$ and improvement coefficients as specified in Ref. [49]. Note that the one-loop coefficient depends on the number of flavours, $\delta am_{\text{cr}}^{(1)} = \delta am_{\text{cr}}^{(1,0)} + \delta am_{\text{cr}}^{(1,1)} N_f$, with numerical values taken from [49].

B.1.1 Bare parameters

For the 9 highest temperatures T_0, \dots, T_8 , we opted for the Wilson plaquette action in Eq. (20). This allows us to fix the bare parameters along the lines of constant physics by exploiting the known results for the SF coupling computed de facto at the critical mass. For $L_0/a = 6, 8, 10$ they are given in Table 3 of Ref. [34], while those for $L_0/a = 4$ were given to us by the authors of that reference as a private communication. For each value of L_0/a , we can determine the values of β at which the SF coupling has the prescribed values reported in Table 2 by fitting $\bar{g}_{\text{SF}}^2(\mu)$ to the functional form

$$\frac{1}{\bar{g}_{\text{SF}}^2} = \frac{1}{g_0^2} + \sum_{k=0}^{n_p} c_k g_0^{2k}. \quad (38)$$

For $L_0/a = 4$ we have fitted 16 data points in the ranges $\bar{g}_{\text{SF}}^2 = 2.0451\text{--}1.1077$ and $\beta = 5.9949\text{--}8.3130$ with $n_p = 3$ obtaining $\chi^2/\text{dof} \approx 1$. The results for the interpolated β -values are reported in Table 4. For $L_0/a = 6, 8$, the values of β reported in Table 4 are taken from Table 6 of Ref. [35], which were obtained by interpolating the data of Ref. [34] as well. As an independent check, we performed our own fits using the functional form in Eq. (38) with $n_p = 2$ including always all available data. We obtained $\chi^2/\text{dof} = 0.38$ and 0.74 for $L_0/a = 6, 8$ respectively. For the interpolated β -values we find excellent agreement within errors between the determinations of Ref. [35] and our results. We decided to take as central values the results of this reference as this will allow us in the future to directly profit from the determination of renormalization factors obtained on the ensembles generated in Ref. [35]. The 6 data points for $L_0/a = 10$ have been fitted to the functional form in Eq. (38) with $n_p = 2$ obtaining $\chi^2/\text{dof} \approx 0.7$. The interpolated β -values are again reported in Table 4.

T	L_0/a	β	$\kappa_{\text{cr}}^{(W)}$	$c_{\text{sw}}^{(W)}$
T_0	4	8.7325	0.131887597685602	1.224666388699756
	6	8.9950	0.131885781718599	1.214293680665697
T_1	4	8.3033	0.132316223701646	1.244443949720750
	6	8.5403	0.132336064110711	1.233045285565058
	8	8.7325	0.132133744093735	1.224666388699756
	10	8.8727	0.131984877002653	1.218983546266290
T_2	4	7.9794	0.132672230374640	1.262303345977765
	6	8.2170	0.132690343212428	1.248924515099129
	8	8.4044	0.132476707113024	1.239426196162344
	10	8.5534	0.132305706323476	1.232451001338001
T_3	4	7.6713	0.133039441274476	1.282333503658225
	6	7.9091	0.133057201010874	1.266585617959733
	8	8.0929	0.132831173856378	1.255711356539447
	10	8.2485	0.132638399517155	1.247267216254281
T_4	4	7.3534	0.133449711446233	1.307002958449583
	6	7.5909	0.133469338865844	1.288146969458134
	8	7.7723	0.133228362183550	1.275393611340024
	10	7.9322	0.133013578229002	1.265160978064686
T_5	4	7.0250	0.133908723921720	1.338089264736139
	6	7.2618	0.133933679858703	1.315030958783770
	8	7.4424	0.133674531074371	1.299622821237046
	10	7.6042	0.133438165920285	1.287166774665371
T_6	4	6.7079	0.134386271436463	1.375352693193284
	6	6.9433	0.134421953633166	1.346919223092444
	8	7.1254	0.134141768774467	1.327878356622864
	10	7.2855	0.133888442235086	1.312909828079458
T_7	4	6.3719	0.134926677491050	1.425561566301377
	6	6.6050	0.134982857878749	1.389385004928746
	8	6.7915	0.134676613758678	1.364706438701718
	10	6.9453	0.134412950133538	1.346697162567041
T_8	4	6.0433	0.135481632961481	1.489790983990814
	6	6.2735	0.135571353236717	1.442967721668930
	8	6.4680	0.135236172024848	1.409845308468962
	10	6.6096	0.134976206524104	1.388734449325687

Table 4: Parameters of the Monte Carlo simulations performed with the Wilson plaquette action. The bare gauge coupling is expressed in terms of $\beta = 6/g_0^2$.

Since $T_0 = 2T_1$, the β -value of $L_0/a = 4$ is the one for T_1 at $L_0/a = 8$, while the β -value of $L_0/a = 6$ corresponds to the one for $L_0/a = 12$ at $\bar{g}_{\text{SF}}^2 = 1.11$ from Table 6 in Ref. [35].

Once defined the lines of constant physics, the values of the critical mass have been determined from Ref. [50]. They fix m_{cr} by requiring that the PCAC mass, computed in a finite volume with SF boundary conditions, vanishes, see Ref. [50] for more details. They get

$$am_{\text{cr}}(g_0^2, a/L_0) = am_{\text{cr}}^{2\text{lp}}(g_0^2, a/L_0) + c_1^{L/a} g_0^6 + c_2^{L/a} g_0^8 + c_3^{L/a} g_0^{10},$$

T	$\bar{g}_{\text{GF}}^2(\mu = T/\sqrt{2})$	T (GeV)
T_9	2.7359	2.833(68)
T_{10}	3.2029	1.821(39)
T_{11}	3.8643	1.167(23)

Table 5: Values of the GF couplings corresponding to the lines of constant physical temperature that we consider.

were the coefficients $c_i^{L/a}$, $i = 1, 2, 3$, are given in Ref. [50]. The rest of the expression corresponds to the two-loop critical mass,

$$am_{\text{cr}}^{2\text{lp}}(g_0^2, a/L_0) = (am_{\text{cr}}^{(0)} + \delta am_{\text{cr}}^{(0)}(a/L_0)) + (am_{\text{cr}}^{(1)} + \delta am_{\text{cr}}^{(1)}(a/L_0)) g_0^2 + am_{\text{cr}}^{(2)} g_0^4, \quad (39)$$

where

$$am_{\text{cr}}^{(0)} = 0, \quad am_{\text{cr}}^{(1)} = -0.270075349459, \quad am_{\text{cr}}^{(2)} = -0.039772, \quad (40)$$

are the asymptotic coefficients in the limit $L_0/a \rightarrow \infty$ while Table 3 contains the coefficients due to cutoff effects. The interpolated values for $\kappa_{\text{cr}} = 2am_{\text{cr}} + 8$ as well as those for c_{sw} obtained from Eq. (39) and Eq. (31) respectively are reported in Table 4 and are indicated with $\kappa_{\text{cr}}^{(W)}$ and $c_{\text{sw}}^{(W)}$.

B.2 Low temperatures

The lower temperature values T_9, T_{10} and T_{11} are fixed analogously to the higher ones but from the gradient flow (GF) coupling. The temperature is fixed by imposing that

$$T = \frac{1}{L_0\sqrt{2}} = \sqrt{2}\mu, \quad (41)$$

where μ is the renormalization scale of the GF coupling $\bar{g}_{\text{GF}}^2(\mu)$ defined in a box with spatial and temporal extensions satisfying $L^{\text{GF}} = L_0^{\text{GF}} = 1/\mu$, i.e. $L_0 = L_0^{\text{GF}}/2$.

In order to determine the physical values of the temperature, we start from the result (cf. Eqs. (15)-(16) and Tables I-II of Ref. [39]),

$$\bar{g}_{\text{GF}}^2(\mu_{\text{had},1}) = 11.31 \quad \Rightarrow \quad \mu_{\text{had},1} = 196.9(3.2) \text{ MeV}, \quad (42)$$

where $\mu_{\text{had},1}$ is inferred from the experimental value of a combination of the pion and kaon decay constant as for μ_0 . The value of the temperatures corresponding to the couplings of interest can then be inferred through the relation,

$$\ln\left(\frac{\mu}{\mu_{\text{had},1}}\right) = \int_{\bar{g}_{\text{GF}}(\mu_{\text{had},1})}^{\bar{g}_{\text{GF}}(\mu)} \frac{dg}{\beta_{\text{GF}}(g)}, \quad (43)$$

where

$$\mu \frac{d\bar{g}_{\text{GF}}(\mu)}{d\mu} = \beta_{\text{GF}}(\bar{g}_{\text{GF}}). \quad (44)$$

Using the results of Ref. [33], the non-perturbative β -function of the GF coupling can be parameterized over the range of couplings of interest as (cf. Eq. (2.36) of Ref. [35])

$$\beta_{\text{GF}}(\bar{g}) = -\frac{\bar{g}^3}{\sum_{n=0}^2 p_n \bar{g}^{2n}}, \quad \bar{g}^2 \in [2.1, 11.3], \quad (45)$$

with fit parameters

$$p_0 = 16.07, \quad p_1 = 0.21, \quad p_2 = -0.013, \quad (46)$$

and covariance matrix

$$\text{cov}(p_i, p_j) = \begin{pmatrix} 5.12310 \times 10^{-1} & -1.77401 \times 10^{-1} & 1.32026 \times 10^{-2} \\ -1.77401 \times 10^{-1} & 6.60392 \times 10^{-2} & -5.10305 \times 10^{-3} \\ 1.32026 \times 10^{-2} & -5.10305 \times 10^{-3} & 4.06114 \times 10^{-4} \end{pmatrix}. \quad (47)$$

Given this representation, we integrated Eq. (43) numerically using the result for $\mu_{\text{had},1}$ in Eq. (42), the relation Eq. (41), and the values for the coupling in Table 5 where are also reported the final values of the temperatures T_9, T_{10} and T_{11} .

B.2.1 Bare parameters

For the 3 lowest temperatures T_9, T_{10} and T_{11} we adopted the tree-level Symanzik improved gauge action in Eq. (32) so as to be able to use the results from Ref. [33] on the GF coupling, $\bar{g}_{\text{GF}}^2(\mu)$, computed in the massless theory.

For each value of L_0/a , the bare parameters are taken from Table 8 of Ref. [35] and are reported in Table 7. To verify that the temperature is constant within each set, we have fitted the results in Table 1 of Ref. [33] for each value of L_0/a using the functional form in Eq. (38) but with $\bar{g}_{\text{SF}}^2(\mu)$ replaced by $\bar{g}_{\text{GF}}^2(\mu)$ and by taking into account that in this case $\mu = 1/(2L_0)$. By including all the 9 data points for each value of L_0/a , and by choosing $n_p = 2$ for $L_0/a = 4, 6$, and $n_p = 3$ for $L_0/a = 8$, we obtained excellent fits with $\chi^2/\text{dof} \approx 0.93, 0.16$ and 1.07 for $L_0/a = 4, 6$ and 8 respectively. The results confirm that the temperature is constant within errors for the lattices within each set.

Once the lines of constant physics have been defined, the corresponding values of the critical mass have been computed from the result in Appendix A.1.4 of Ref. [33] which reads

$$am_{\text{cr}}(g_0^2, a/L_0) = \left(\sum_{k=0}^6 \mu_k g_0^{2k} \right) \times \left(\sum_{i=0}^6 \zeta_i g_0^{2i} \right)^{-1}, \quad (48)$$

with the parameters μ_k and ζ_i listed in Table 6 for the relevant L_0/a . As for the case of the Wilson-plaquette gauge action, the values of $m_{\text{cr}}(g_0^2, a/L_0)$ depend on L_0/a because it has been determined by requesting the PCAC mass to vanish in a finite volume, see Ref. [33] for more details.

Once the β -values have been determined, the corresponding values for $\kappa_{\text{cr}} = 2am_{\text{cr}} + 8$ as well as those for c_{sw} are obtained from Eqs. (48) and (32) respectively, and are reported in Table 7 as $\kappa_{\text{cr}}^{(I)}$ and $c_{\text{sw}}^{(I)}$.

Coeff.	$L_0/a = 4$	$L_0/a = 6$	$L_0/a = 8$
ζ_0	+1.005834130000000	+1.002599440000000	+1.001463290000000
μ_0	-0.000022208694999	-0.000004812471537	-0.000001281872601
μ_1	-0.202388398516844	-0.201746020772477	-0.201520105247962
ζ_1	-0.560665657872021	-0.802266237327923	-0.892637061391273
ζ_2	+3.262872842957498	+4.027758778155415	+5.095631719496583
ζ_3	-5.788275397637978	-6.928207214808553	-8.939546687871335
ζ_4	+4.587959856400246	+5.510985771180077	+7.046607832794273
ζ_5	-1.653344785588201	-2.076308895962694	-2.625638312722623
ζ_6	+0.227536321065082	+0.320430672213824	+0.405387660384441
μ_2	+0.090366980657738	+0.128161834555849	+0.139461345465939
μ_3	-0.600952105402754	-0.681097059845447	-0.847457204378732
μ_4	+0.934252532135398	+0.991316994385556	+1.261676178806362
μ_5	-0.608706158693056	-0.606597739050552	-0.754644691612547
μ_6	+0.140501978953879	+0.129031928169091	+0.153135714480269

Table 6: Coefficients for the parameterization Eq. (48). The three leading coefficients ζ_0 , μ_0 , and μ_1 in the upper part of the table are combinations of known perturbative coefficients while the others were determined by a fit.

T	L_0/a	β	$\kappa_{\text{cr}}^{(I)}$	$c_{\text{sw}}^{(I)}$
T_9	4	4.764900	0.134885548000448	1.335350323996506
	6	4.938726	0.134507608658235	1.308983384364439
	8	5.100000	0.134168886219319	1.288203306487197
T_{10}	4	4.457600	0.135606746160064	1.39574103127591
	6	4.634654	0.135199857298424	1.358462476494125
	8	4.800000	0.134821158536685	1.329646151978636
T_{11}	4	4.151900	0.136325892438363	1.482418125298923
	6	4.331660	0.135926636004668	1.427424655158656
	8	4.500000	0.135525721037715	1.386110343557152

Table 7: Parameters of the Monte Carlo simulations performed with the tree-level improved Symanzik action. The bare gauge coupling is expressed in terms of $\beta = 6/g_0^2$.

C Finite-volume effects in thermal two-point correlators

In this appendix we derive the formula for the leading finite-volume effects in the spatial correlators $C_{\mathcal{O}}(x_3)$ defined in Eq. (7) at asymptotically high temperatures. We follow the lines of argumentation in Refs. [25, 36, 51], and we assume the reader to be familiar with these papers. Gauge and quark fields are assumed to satisfy shifted boundary conditions, Eqs. (10) and (11), with $\xi = (\xi_1, 0, 0)$. In the continuum theory, where finite volume effects are derived, the results can be readily generalized to a generic shift ξ by exploiting the invariance of the theory under the $SO(3)$ spatial rotations, see Ref. [25] for details.

We start by considering a box of volume $L_0 \times L^3$, and we define the finite-volume residue due to the compactification in the 1-direction as

$$\mathcal{I}_1(x_3, L) \equiv \left[1 - \lim_{L_1 \rightarrow \infty} \right] C_{\mathcal{O}}(x_3), \quad (49)$$

where L_1 is the length of the box in direction 1. In order to determine \mathcal{I}_1 we consider the

transfer-matrix representation of $C_{\mathcal{O}}(x_3)$ along the 1-direction (cf. Sect. 4 of Ref. [25]),

$$C_{\mathcal{O}}(x_3) = \int dx_0 dx_1 dx_2 \frac{\text{Tr}[e^{-(L\gamma_1 - x_1)\tilde{H}} \mathcal{O}^a(\tilde{\mathbf{x}}) e^{-x_1\tilde{H}} \mathcal{O}^a(\tilde{\mathbf{0}}) e^{-iL\gamma_1\xi_1\tilde{\omega}}]}{\text{Tr}[e^{-L\gamma_1(\tilde{H} + i\xi_1\tilde{\omega})}]}, \quad (50)$$

where $\tilde{\mathbf{x}} = (x_0, x_2, x_3)$, $\gamma_1 = (1 + \xi_1^2)^{-1/2}$, and the trace Tr is carried over the states of the corresponding Hilbert space. In this equation, \tilde{H} stands for the screening Hamiltonian along the 1-direction. This operator has a discrete spectrum of states defined on a slice of dimensions $(L_0/\gamma_1) \times L \times L$, with ordinary periodic boundary conditions. The operator $\tilde{\omega}$ denotes instead the momentum operator along the 0-direction of length (L_0/γ_1) . We indicate with $|n\rangle$ the simultaneous eigenstates of \tilde{H} , $\tilde{\omega}$, and potentially other conserved charge operators. The eigenvalues of \tilde{H} and $\tilde{\omega}$ corresponding to the state $|n\rangle$ are the energies E_n and Matsubara frequencies $\omega_n = 2\pi m_n \gamma_1 / L_0$, $m_n \in \mathbb{Z}$, respectively. We assume that the states are ordered in such a way that $E_{n+1} \geq E_n$. The state $|0\rangle$ is therefore the unique ground state of the system, for which we conveniently set $E_0 = 0$. At asymptotically high temperature, the state $|1\rangle$ is then expected to have a strictly positive mass(-gap), M_{gap} , proportional to the temperature T , see section 2. Furthermore, due to the fact that at asymptotically high temperature the effective theory of QCD contains only purely gluonic degrees of freedom, we expect the lowest-lying energy states, i.e. those with $E_n \ll \pi T$, to have zero flavour quantum-numbers [17]. Inserting two complete sets of eigenstates $|n\rangle$ with zero baryon number in Eq. (50), we have

$$C_{\mathcal{O}}(x_3) = \frac{1}{Z} \int dx_0 dx_1 dx_2 \sum_{n, n'} e^{-L\gamma_1(E_n + i\xi_1\omega_n)} e^{-x_1(E_{n'} - E_n)} \langle n | \mathcal{O}^a(\tilde{\mathbf{x}}) | n' \rangle \langle n' | \mathcal{O}^a(\tilde{\mathbf{0}}) | n \rangle + \dots, \quad (51)$$

where $Z = \sum_n e^{-L\gamma_1(E_n + i\xi_1\omega_n)} + \dots$, and the dots stand for baryonic contributions which are suppressed exponentially with respect to the sum. Let us focus on the terms in the sum for which $E_n \neq E_{n'}$. For these, the integral over x_1 gives

$$e^{-L\gamma_1 E_n} \int_0^{L\gamma_1} dx_1 e^{-x_1(E_{n'} - E_n)} = \frac{e^{-L\gamma_1 E_n} - e^{-L\gamma_1 E_{n'}}}{E_{n'} - E_n}. \quad (52)$$

Inserting this relation in Eq. (51), and relabeling $n \leftrightarrow n'$ in some terms, we obtain

$$C_{\mathcal{O}}(x_3) = \frac{1}{Z} \int dx_0 dx_2 \sum_{\substack{n, n' \\ E_n \neq E_{n'}}} \frac{e^{-L\gamma_1(E_n + i\xi_1\omega_n)}}{E_{n'} - E_n} \times \\ \times \left\{ \langle n | \mathcal{O}^a(\tilde{\mathbf{x}}) | n' \rangle \langle n' | \mathcal{O}^a(\tilde{\mathbf{0}}) | n \rangle + \langle n | \mathcal{O}^a(\tilde{\mathbf{0}}) | n' \rangle \langle n' | \mathcal{O}^a(\tilde{\mathbf{x}}) | n \rangle \right\} + \dots, \quad (53)$$

where the terms with $E_n = E_{n'}$ are included in the dots.³ In this form, it is evident that in the limit where $L_1 \rightarrow \infty$, the terms with energies $E_n \ll \pi T$ dominate the sum. Furthermore, within this energy range, there are no terms with $E_n = E_{n'}$ that can contribute. This is because the operators \mathcal{O}^a have non-trivial flavour quantum-numbers and any flavoured mesonic state has an energy $E_n \gtrsim 2\pi T$. As we are interested in determining the leading finite-volume effects in $C_{\mathcal{O}}(x_3)$, from now on we shall restrict ourselves to consider only states

³Note that in order to derive Eq. (53) we used the fact that $C_{\mathcal{O}}(x_3)$ is projected onto zero Matsubara frequency and therefore $\omega_n = \omega_{n'}$.

that satisfy the above energy constraint. These include, in particular, the theory vacuum and the 1-particle states with mass equal to the mass-gap M_{gap} . We can thus introduce the two-point correlation function

$$G_n(\tau, \tilde{\mathbf{x}}) = \langle n | \text{T} \{ \mathcal{O}^a(\tau, \tilde{\mathbf{x}}) \mathcal{O}^a(0, \tilde{\mathbf{0}}) \} | n \rangle, \quad (54)$$

where $\text{T}\{\dots\}$ stands for the ordered product of the operators with respect to the parameter τ , and $\mathcal{O}^a(\tau, \tilde{\mathbf{x}}) = e^{\tau \tilde{H}} \mathcal{O}^a(\tilde{\mathbf{x}}) e^{-\tau \tilde{H}}$. After some trivial algebra, it is immediate to show that,

$$\int_{-\infty}^{\infty} d\tau G_n(\tau, \tilde{\mathbf{x}}) = \sum_{n'} \frac{1}{E_{n'} - E_n} \left\{ \langle n | \mathcal{O}^a(\tilde{\mathbf{x}}) | n' \rangle \langle n' | \mathcal{O}^a(\tilde{\mathbf{0}}) | n \rangle + \langle n | \mathcal{O}^a(\tilde{\mathbf{0}}) | n' \rangle \langle n' | \mathcal{O}^a(\tilde{\mathbf{x}}) | n \rangle \right\}. \quad (55)$$

Considering the $L_1 \rightarrow \infty$ limit of Eq. (53), and using the above relation, we find for \mathcal{I}_1 the result

$$\mathcal{I}_1(x_3, L) = \sum_{n \mid \substack{\text{1-particle} \\ \text{states}}} e^{-L\gamma_1(E_n + i\xi_1\omega_n)} \int dx_0 dx_2 d\tau \{ G_n(\tau, \tilde{\mathbf{x}}) - G_0(\tau, \tilde{\mathbf{x}}) \} + \dots, \quad (56)$$

where the energies of the 1-particle states are confined to the range $M_{\text{gap}} \lesssim E_n \lesssim \pi T$ and the dots stand for terms which are exponentially suppressed compared to the leading ones. From this expression, it is immediate to conclude that \mathcal{I}_1 is exponentially suppressed as $M_{\text{gap}}L \rightarrow \infty$. Moreover the length of the other two spatial directions can be sent to infinity on the r.h.s. of Eq. (56) up to sub-leading finite-volume effects. The analogous contribution from the 2-direction, \mathcal{I}_2 , is obtained from the one for \mathcal{I}_1 in Eq. (56) by replacing $L\gamma_1 \rightarrow L$, $\xi_1 \rightarrow 0$, and $x_2 \rightarrow x_1$. (Note that the length of the 0-direction remains L_0/γ_1). Finite-volume corrections in the 3-direction can be taken into account, as usual, by considering the backward propagation in the series of exponentials due to periodic boundary conditions in that direction. The total finite-volume effects in $C_{\mathcal{O}}(x_3)$ are finally given by summing all three contributions. Since the screening masses are extracted at asymptotically large distances according to Eq. (14), their finite-volume corrections are determined by $\mathcal{I}_1 + \mathcal{I}_2$ only.

D Inversion of the Dirac operator

The usual stopping criterion used in iterative methods for the numerical solution of the Dirac equation

$$D\psi = \eta \quad (57)$$

requires that the norm of the residual $\rho = D\psi - \eta$ is sufficiently small, i.e. the global condition $r = \|\rho\|/\|\eta\| < \varepsilon$. The tolerance ε is chosen to be small enough that the error introduced by using such an approximate solution must be negligible with respect to the statistical fluctuations on the observable of interest. However, the tolerance cannot be smaller than what is allowed by the finite-precision arithmetic of a given implementation.

At high temperature, the lowest Matsubara frequency πT provides an infrared cutoff to quark propagation. As a result, the matrix elements $D^{-1}(x, y)$ become extremely small when $T|x - y| \gg 1$, and a very accurate solution of the Dirac equation is required at those distances. The brute-force approach of simply implementing higher-precision and requiring a

smaller tolerance is not always practicable. In this case, a solution is achieved by introducing a preconditioned version of the Dirac equation,

$$\tilde{D}\tilde{\psi} = \tilde{\eta} \quad (58)$$

where

$$\tilde{D} = M^{-1}DM, \quad \tilde{\psi} = M^{-1}\psi, \quad \tilde{\eta} = M^{-1}\eta, \quad (59)$$

with the preconditioning matrix M chosen so that the various components of the solution $\tilde{\psi}$ are comparable in magnitude [52].

The quark propagators needed for the two-point meson correlation functions considered in this paper have been computed by implementing the preconditioning matrix

$$M(x, y) = \cosh\{m_M(x_3 - y_3 - L/2)\} \cdot \mathbb{1}, \quad (60)$$

where $\mathbb{1}$ indicates the identity matrix in the indices not explicitly indicated, i.e. color, spin and the first three components of space-time coordinates. After some tuning, for the lattices with $L_0/a = 4, 6, 8$ and 10 we have chosen $m_M = 0.4, 0.3, 0.2$ and 0.15 respectively, with the shift being always $\boldsymbol{\xi} = (1, 0, 0)$. This indeed guarantees that the components of $\tilde{\psi}$ are always comparable in magnitude. We have also monitored explicitly a posteriori that the global condition $r < \varepsilon$ is always satisfied by the solution vector.

E Simulation details and results

We have simulated three-flavour QCD with a HMC algorithm by using the `openQCD-1.6` package [53, 54] modified so as to allow for shifted boundary conditions. We have employed several efficient algorithms to speed up the simulations. More precisely, the doublet of up and down quarks have been simulated with an optimized twisted-mass Hasenbusch preconditioning of the quark determinant [53, 55]. The determinant has been split in three factors by employing the twisted masses values $a\mu = 0.0, 0.1$ and 1.0 . The strange quark has been simulated through a RHMC algorithm [56, 57] with an optimized frequency splitting of the rational approximation in two separate contributions. Even-odd preconditioning has been used for both the light and strange quarks. The integration of the molecular dynamics equations has been based on a three-level integration scheme. The gauge force has been integrated on the finest level using a 4th-order Omelyan-Mryglod-Folk (OMF4) integrator [58] with step-size 1, while the fermionic forces have been integrated on the two coarser levels. On the finest of these we have used a OMF4 integrator step-size 1, while on the coarsest a 2nd-order OMF integrator [58] with step-size between 7 and 9. The solution of the Dirac equation along the molecular dynamics evolution has been obtained by using a standard conjugate gradient with chronological inversion. The length of each trajectory is 2 MDUs for all lattices. More details on the exact implementation of these algorithms can be found in Refs. [53, 54].

For each ensemble, we have started the thermalization phase by simulating a lattice with a spatial length of $L/a = 48$ in all three directions and the same bare parameters as the target one. After approximately 1000 MDUs, we have duplicated the lattice in each direction so that $L/a = 96$. We have then run the HMC for approximately 500 MDUs, after which we have triplicated the lattice in all spatial directions so to have $L/a = 288$. We have completed the thermalization phase by running the HMC for a number of MDUs between 100 to 200, and then we have started the computation of the correlation functions. During all the phases of

T	L_0/a	n_{mdu}	n_{skip}	n_{nsrc}	$\frac{m_P}{2\pi T}$	$\frac{m_V}{2\pi T}$	$\frac{(m_V - m_P)}{2\pi T}$
T_0	4	90	10	4	0.9659(5)	0.9716(7)	0.00577(20)
	6	90	10	2	0.9934(14)	0.9996(12)	0.0065(4)
T_1	4	90	10	4	0.9656(7)	0.9721(8)	0.0068(3)
	6	270	30	2	0.9945(14)	1.0014(19)	0.0070(8)
	8	450	50	2	1.0078(18)	1.0148(20)	0.0075(5)
	10	900	100	2	1.0090(25)	1.0160(27)	0.0075(4)
T_2	4	90	10	4	0.9685(7)	0.9753(8)	0.0075(3)
	6	270	30	2	0.9961(14)	1.0049(18)	0.0089(5)
	8	450	50	2	1.0055(23)	1.0147(25)	0.0089(5)
	10	900	100	2	1.0122(25)	1.0207(25)	0.0073(6)
T_3	4	90	10	4	0.9682(11)	0.9764(18)	0.0087(5)
	6	270	30	2	0.9971(11)	1.0050(16)	0.0084(10)
	8	450	50	2	1.0039(18)	1.0130(22)	0.0083(7)
	10	810	90	2	1.0124(25)	1.0219(29)	0.0099(7)
T_4	4	90	10	4	0.9704(7)	0.9804(14)	0.0103(4)
	6	270	30	2	0.9973(14)	1.0087(14)	0.0109(8)
	8	450	50	2	1.0051(20)	1.0172(25)	0.0093(9)
	10	540	60	2	1.0138(20)	1.0248(23)	0.0108(7)
T_5	4	90	10	4	0.9708(8)	0.9838(12)	0.0128(4)
	6	180	20	2	0.9941(22)	1.006(3)	0.0109(20)
	8	450	50	2	1.0057(18)	1.0172(29)	0.0119(21)
	10	540	60	2	1.0090(27)	1.0228(29)	0.0137(10)
T_6	4	90	10	4	0.9676(10)	0.9830(18)	0.0156(11)
	6	180	20	2	0.9948(15)	1.0089(24)	0.0142(11)
	8	450	50	2	1.0037(29)	1.018(4)	0.0150(23)
	10	540	60	2	1.0108(25)	1.026(4)	0.0153(16)
T_7	4	90	10	4	0.9679(8)	0.9854(18)	0.0172(11)
	6	180	20	2	0.9930(15)	1.0093(28)	0.0171(17)
	8	450	50	2	1.0051(22)	1.024(4)	0.0188(16)
	10	900	100	2	1.012(3)	1.028(5)	0.0171(19)
T_8	4	90	10	4	0.9677(8)	0.9910(18)	0.0235(17)
	6	180	20	4	0.9907(16)	1.015(4)	0.0237(17)
	8	450	50	4	1.000(3)	1.025(4)	0.0247(14)
	10	900	100	4	1.0032(23)	1.0288(25)	0.0252(14)

Table 8: Results for the pseudoscalar, m_P , and the vector, m_V , non-singlet meson masses together with their difference $(m_V - m_P)$ all normalized to $2\pi T$ at finite lattice spacing for the temperatures T_0, \dots, T_8 . The number of MDUs generated, n_{mdu} , those skipped between two consecutive measurements, n_{skip} , and the number of local sources per configuration on which the two-point correlation functions have been computed, n_{nsrc} , are also reported.

thermalization we have always monitored the action and the various components of the energy-momentum tensor. We have also constantly monitored the topological charge computed with

T	L_0/a	n_{mdu}	n_{skip}	n_{nsrc}	$\frac{m_P}{2\pi T}$	$\frac{m_V}{2\pi T}$	$\frac{(m_V - m_P)}{2\pi T}$
T_9	4	90	10	4	0.9663(16)	0.9872(23)	0.0205(15)
	6	90	10	4	0.9907(24)	1.012(4)	0.0233(27)
	8	90	10	4	1.0010(20)	1.0238(25)	0.0233(16)
T_{10}	4	90	10	4	0.9645(13)	0.9912(17)	0.0259(22)
	6	90	10	4	0.9896(11)	1.0203(24)	0.0294(18)
	8	90	10	4	0.9963(22)	1.024(4)	0.0290(16)
T_{11}	4	90	10	4	0.9552(16)	0.992(3)	0.0375(18)
	6	90	10	8	0.9768(20)	1.018(5)	0.0406(26)
	8	90	10	8	0.9912(16)	1.031(6)	0.039(4)

Table 9: As in Table 8 but for T_9 , T_{10} and T_{11} .

the Wilson flow, and we have explicitly checked that at the end of each thermalization process we always ended up in the trivial topological sector.

Once the thermalization has been concluded, we have accumulated a certain number of configurations for the computation of the EoS. Among those, we have selected some that we have used for the computation of the screening masses. In particular in Tables 8 and 9 we report the number of MDUs considered, the number of MDUs skipped between two consecutive independent configurations, and the number of local sources per configuration on which the two-point correlation functions have been computed. For each configuration, the best estimates of $C_{\mathcal{O}}(x_3)$ in Eq. (13) have been obtained by properly averaging their values from all local sources, and then symmetrizing the correlators with respect to $x_3 = L/2$. The screening masses have then been extracted as described in Section 6. The results are reported in Tables 8 and 9 for the 9 highest temperatures T_0, \dots, T_8 and for the lowest ones, T_9, T_{10} and T_{11} respectively.

To explicitly check that finite volume effects are negligible within our statistical errors, we have generated three more lattices at T_0 ($L_0/a = 6$), T_1 ($L_0/a = 10$) and T_{11} ($L_0/a = 8$) at three smaller spatial volumes, namely $6 \times 144^2 \times 288$, $10 \times 96^2 \times 288$, and $8 \times 144^2 \times 288$ (direction 3 the longest) respectively. On these lattices we have computed the screening masses following the same procedure as described before. They are in very good agreement with the analogous ones reported in Tables 8 and 9, and therefore they confirm the theoretical expectations that finite volume effects are negligible.

F Screening masses in the free lattice theory

With the aim of accelerating the continuum limit extrapolation, we report here the calculation of the non-singlet meson screening masses in the free theory on the lattice. Since D_{sw} in Eq. (25) does not contribute in the free case, the quark propagator in momentum space for each single flavour is given by

$$S(p) = \frac{-i\gamma_\mu \bar{p}_\mu + m_0(p)}{D_F(p)}, \quad \text{with} \quad D_F(p) = \sum_{\mu=0}^3 \bar{p}_\mu^2 + m_0^2(p) \quad (61)$$

L_0/a	$m^{\text{free}}/(2\pi T)$
4	0.932614077...
6	0.967811412...
8	0.981401809...
10	0.987944825...

Table 10: Tree-level values of the non-singlet screening masses on lattices with temporal extension L_0/a , infinite spatial volume, and shift vector $\boldsymbol{\xi} = (1, 0, 0)$.

and

$$m_0(p) = m_0 + \frac{a}{2} \sum_{\mu=0}^3 \hat{p}_\mu^2, \quad \bar{p}_\mu = \frac{1}{a} \sin(ap_\mu), \quad \hat{p}_\mu = \frac{2}{a} \sin\left(\frac{ap_\mu}{2}\right), \quad (62)$$

where we have assumed $M_0 = m_0 \cdot \mathbb{1}$. In the presence of shifted boundary conditions (see appendices A and E in [27]), the fermionic lattice momenta in the compact direction take the values

$$p_0 = \frac{2\pi n_0}{L_0} + \frac{\pi}{L_0} - \sum_{k=1}^3 p_k \xi_k \quad \text{where } n_0 = 0, \dots, L_0/a - 1 \quad (63)$$

while in the spatial directions we consider the infinite volume limit and therefore the momenta are given by $p_k \in [-\pi/a, \pi/a)$.

To extract the screening masses, we compute the two-point correlators defined in Eq. (7) for $\mathcal{O} = \{S, P, V_\mu, A_\mu\}$ corresponding to $\Gamma_{\mathcal{O}} = \{\mathbb{1}, \gamma_5, \gamma_\mu, \gamma_\mu \gamma_5\}$ respectively. At tree-level they are given by

$$C_{\mathcal{O}}(x_3) = -\frac{3}{2} \int \frac{d^4 p}{(2\pi)^4} \frac{dk_3}{2\pi} \text{Tr} \left[\Gamma_{\mathcal{O}} S(k) \Gamma_{\mathcal{O}} S(p) \right] e^{-i(p_3 - k_3)x_3}, \quad (64)$$

where $k = (p_0, p_1, p_2, k_3)$ and Tr stands for the trace over the Dirac index. From Eq. (3.613 – 1.6) of Ref. [59] we obtain

$$\int \frac{dp_3}{2\pi} \frac{e^{-ip_3 x_3}}{D_F(p)} = \frac{e^{-2\hat{\omega}(p)x_3}}{a\omega(p)\bar{\omega}(p)} \quad (65)$$

where

$$\omega^2(p) = \bar{m}^2(p) + \sum_{\nu=0}^2 \bar{p}_\nu^2, \quad \bar{\omega}^2(p) = \left[\bar{m}(p) + \frac{2}{a} \right]^2 + \sum_{\nu=0}^2 \bar{p}_\nu^2, \quad (66)$$

$$\bar{m}(p) = m_0 + \frac{a}{2} \sum_0^2 \hat{p}_n^2, \quad a\hat{\omega}(p) = \frac{1}{2} \ln \left[\frac{\bar{\omega}(p) + \omega(p)}{\bar{\omega}(p) - \omega(p)} \right]. \quad (67)$$

By using the above formulas, one finds that

$$C_{\mathcal{O}}(x_3) = -\frac{3}{a^2 L_0} \sum_{n_0} \int dp_1 dp_2 \bar{C}_{\mathcal{O}}(p) e^{-4\hat{\omega}(p)x_3} \quad (68)$$

where

$$\bar{C}_S(p) = -\frac{4 \sum_{\nu=0}^2 \bar{p}_\nu^2}{\omega^2(p)\bar{\omega}^2(p)}, \quad \bar{C}_{V_\mu}(p) = (1 - \delta_{\mu 3}) \left[\frac{1}{[\bar{m}(p) + 1/a]^2} - \frac{4\bar{p}_\mu^2}{\omega^2(p)\bar{\omega}^2(p)} \right], \quad (69)$$

$$\bar{C}_P(p) = \frac{1}{[\bar{m}(p) + 1/a]^2}, \quad \bar{C}_{A_\mu}(p) = -\frac{\delta_{\mu 3}}{[\bar{m}(p) + 1/a]^2} + \frac{4 \sum_{\nu \neq \mu, 3} \bar{p}_\nu^2}{\omega^2(p) \bar{\omega}^2(p)}. \quad (70)$$

Notice that $\bar{C}_S + \bar{C}_P = \bar{C}_{V_\mu} - \bar{C}_{A_\mu}$. For the shift vector $\boldsymbol{\xi} = (1, 0, 0)$, the minimum of $\hat{\omega}$ is attained for $(p_0, p_1, p_2) = (\frac{\pi}{2L_0}, \frac{\pi}{2L_0}, 0)$ for all correlators we are interested in. The tree-level values of the screening masses are therefore all the same. They are given by the expression

$$m_{\mathcal{O}}^{\text{free}} = 4\hat{\omega}\left(\frac{\pi}{2L_0}, \frac{\pi}{2L_0}, 0\right), \quad (71)$$

whose values normalized to $2\pi T$ are listed, for practical convenience, in Table 10 for the temporal extensions L_0/a relevant to this paper.

References

- [1] P. H. Ginsparg, *First Order and Second Order Phase Transitions in Gauge Theories at Finite Temperature*, *Nucl. Phys. B* **170** (1980) 388–408.
- [2] T. Appelquist and R. D. Pisarski, *High-Temperature Yang-Mills Theories and Three-Dimensional Quantum Chromodynamics*, *Phys. Rev. D* **23** (1981) 2305.
- [3] A. D. Linde, *Infrared Problem in Thermodynamics of the Yang-Mills Gas*, *Phys. Lett. B* **96** (1980) 289–292.
- [4] E. Braaten and A. Nieto, *Free energy of QCD at high temperature*, *Phys. Rev. D* **53** (1996) 3421–3437, [[hep-ph/9510408](#)].
- [5] K. Kajantie, M. Laine, K. Rummukainen, and Y. Schröder, *Pressure of hot qcd up to $g^6 \ln(1/g)$* , *Phys. Rev. D* **67** (May, 2003) 105008.
- [6] L. Giusti and M. Pepe, *Equation of state of the SU(3) Yang–Mills theory: A precise determination from a moving frame*, *Phys. Lett.* **B769** (2017) 385–390, [[arXiv:1612.00265](#)].
- [7] M. Laine and M. Vepsalainen, *Mesonic correlation lengths in high temperature QCD*, *JHEP* **02** (2004) 004, [[hep-ph/0311268](#)].
- [8] V. Koch, E. V. Shuryak, G. E. Brown, and A. D. Jackson, *The Propagation of quarks in the spatial direction in hot QCD*, *Phys. Rev. D* **46** (1992) 3169, [[hep-ph/9204236](#)]. [Erratum: *Phys.Rev.D* 47, 2157 (1993)].
- [9] T. H. Hansson and I. Zahed, *Hadronic correlators in hot QCD*, *Nucl. Phys. B* **374** (1992) 277–287.
- [10] M. Cheng et al., *Meson screening masses from lattice QCD with two light and the strange quark*, *Eur. Phys. J. C* **71** (2011) 1564, [[arXiv:1010.1216](#)].
- [11] B. B. Brandt, A. Francis, M. Laine, and H. B. Meyer, *A relation between screening masses and real-time rates*, *JHEP* **05** (2014) 117, [[arXiv:1404.2404](#)].
- [12] A. Bazavov et al., *Meson screening masses in (2+1)-flavor QCD*, *Phys. Rev. D* **100** (2019), no. 9 094510, [[arXiv:1908.09552](#)].

- [13] B. B. Brandt, O. Philipsen, M. Cè, A. Francis, T. Harris, H. B. Meyer, and H. Wittig, *Testing the strength of the $U_A(1)$ anomaly at the chiral phase transition in two-flavour QCD*, *PoS CD2018* (2019) 055, [[arXiv:1904.02384](#)].
- [14] M. Laine and A. Vuorinen, *Basics of Thermal Field Theory*, vol. 925. Springer, 2016.
- [15] M. Laine and Y. Schröder, *Two-loop QCD gauge coupling at high temperatures*, *JHEP* **03** (2005) 067, [[hep-ph/0503061](#)].
- [16] P. B. Arnold and L. G. Yaffe, *The NonAbelian Debye screening length beyond leading order*, *Phys. Rev. D* **52** (1995) 7208–7219, [[hep-ph/9508280](#)].
- [17] M. Laine and M. Vepsalainen, *On the smallest screening masses in hot QCD*, *JHEP* **09** (2009) 023, [[arXiv:0906.4450](#)].
- [18] S.-z. Huang and M. Lissia, *The Dimensionally reduced effective theory for quarks in high temperature QCD*, *Nucl. Phys. B* **480** (1996) 623–654, [[hep-ph/9511383](#)].
- [19] T. W. Appelquist, M. J. Bowick, D. Karabali, and L. C. R. Wijewardhana, *Spontaneous Chiral Symmetry Breaking in Three-Dimensional QED*, *Phys. Rev. D* **33** (1986) 3704.
- [20] L. Giusti and M. Lüscher, *Topological susceptibility at $T > T_c$ from master-field simulations of the $SU(3)$ gauge theory*, *Eur. Phys. J. C* **79** (2019), no. 3 207, [[arXiv:1812.02062](#)].
- [21] D. J. Gross, R. D. Pisarski, and L. G. Yaffe, *QCD and Instantons at Finite Temperature*, *Rev. Mod. Phys.* **53** (1981) 43.
- [22] A. Boccaletti and D. Negradi, *The semi-classical approximation at high temperature revisited*, *JHEP* **03** (2020) 045, [[arXiv:2001.03383](#)].
- [23] L. Giusti and H. B. Meyer, *Thermodynamic potentials from shifted boundary conditions: the scalar-field theory case*, *JHEP* **11** (2011) 087, [[arXiv:1110.3136](#)].
- [24] L. Giusti and H. B. Meyer, *Thermal momentum distribution from path integrals with shifted boundary conditions*, *Phys. Rev. Lett.* **106** (2011) 131601, [[arXiv:1011.2727](#)].
- [25] L. Giusti and H. B. Meyer, *Implications of Poincare symmetry for thermal field theories in finite-volume*, *JHEP* **01** (2013) 140, [[arXiv:1211.6669](#)].
- [26] L. Giusti and M. Pepe, *Equation of state of a relativistic theory from a moving frame*, *Phys. Rev. Lett.* **113** (2014) 031601, [[arXiv:1403.0360](#)].
- [27] M. Dalla Brida, L. Giusti, and M. Pepe, *Non-perturbative definition of the QCD energy-momentum tensor on the lattice*, *JHEP* **04** (2020) 043, [[arXiv:2002.06897](#)].
- [28] M. Lüscher, P. Weisz, and U. Wolff, *A numerical method to compute the running coupling in asymptotically free theories*, *Nucl. Phys.* **B359** (1991) 221–243.
- [29] K. Jansen et al., *Non-perturbative renormalization of lattice QCD at all scales*, *Phys. Lett.* **B372** (1996) 275–282, [[hep-lat/9512009](#)].

- [30] M. Lüscher, R. Sommer, P. Weisz, and U. Wolff, *A precise determination of the running coupling in the $SU(3)$ Yang-Mills theory*, *Nucl. Phys.* **B413** (1994) 481–502, [[hep-lat/9309005](#)].
- [31] P. Fritzsche and A. Ramos, *Studying the gradient flow coupling in the Schrödinger functional*, *PoS Lattice2013* (2014) 319, [[arXiv:1308.4559](#)].
- [32] **ALPHA** Collaboration, M. Dalla Brida, P. Fritzsche, T. Korzec, A. Ramos, S. Sint, and R. Sommer, *Determination of the QCD Λ -parameter and the accuracy of perturbation theory at high energies*, *Phys. Rev. Lett.* **117** (2016), no. 18 182001, [[arXiv:1604.06193](#)].
- [33] **ALPHA** Collaboration, M. Dalla Brida, P. Fritzsche, T. Korzec, A. Ramos, S. Sint, and R. Sommer, *Slow running of the Gradient Flow coupling from 200 MeV to 4 GeV in $N_f = 3$ QCD*, *Phys. Rev. D* **95** (2017), no. 1 014507, [[arXiv:1607.06423](#)].
- [34] **ALPHA** Collaboration, M. Dalla Brida, P. Fritzsche, T. Korzec, A. Ramos, S. Sint, and R. Sommer, *A non-perturbative exploration of the high energy regime in $N_f = 3$ QCD*, *Eur. Phys. J. C* **78** (2018), no. 5 372, [[arXiv:1803.10230](#)].
- [35] **ALPHA** Collaboration, I. Campos, P. Fritzsche, C. Pena, D. Preti, A. Ramos, and A. Vladikas, *Non-perturbative quark mass renormalisation and running in $N_f = 3$ QCD*, *Eur. Phys. J. C* **78** (2018), no. 5 387, [[arXiv:1802.05243](#)].
- [36] H. B. Meyer, *Finite Volume Effects in Thermal Field Theory*, *JHEP* **07** (2009) 059, [[arXiv:0905.1663](#)].
- [37] C. Bonati, M. D’Elia, M. Mariti, G. Martinelli, M. Mesiti, F. Negro, F. Sanfilippo, and G. Villadoro, *Axion phenomenology and θ -dependence from $N_f = 2 + 1$ lattice QCD*, *JHEP* **03** (2016) 155, [[arXiv:1512.06746](#)].
- [38] S. Borsanyi et al., *Calculation of the axion mass based on high-temperature lattice quantum chromodynamics*, *Nature* **539** (2016), no. 7627 69–71, [[arXiv:1606.07494](#)].
- [39] **ALPHA** Collaboration, M. Bruno, M. Dalla Brida, P. Fritzsche, T. Korzec, A. Ramos, S. Schaefer, H. Simma, S. Sint, and R. Sommer, *QCD Coupling from a Nonperturbative Determination of the Three-Flavor Λ Parameter*, *Phys. Rev. Lett.* **119** (2017), no. 10 102001, [[arXiv:1706.03821](#)].
- [40] K. G. Wilson, *Confinement of Quarks*, *Phys. Rev. D* **10** (1974) 2445–2459.
- [41] M. Lüscher and P. Weisz, *On-Shell Improved Lattice Gauge Theories*, *Commun. Math. Phys.* **97** (1985) 59. [Erratum: *Commun. Math. Phys.*98,433(1985)].
- [42] K. G. Wilson, *Quarks: From Paradox to Myth*, *Subnucl. Ser.* **13** (1977) 13–32.
- [43] B. Sheikholeslami and R. Wohlert, *Improved Continuum Limit Lattice Action for QCD with Wilson Fermions*, *Nucl. Phys.* **B259** (1985) 572.
- [44] M. Lüscher, S. Sint, R. Sommer, and P. Weisz, *Chiral symmetry and $O(a)$ improvement in lattice QCD*, *Nucl. Phys.* **B478** (1996) 365–400, [[hep-lat/9605038](#)].

- [45] **JLQCD, CP-PACS** Collaboration, N. Yamada et al., *Non-perturbative $O(a)$ -improvement of Wilson quark action in three-flavor QCD with plaquette gauge action*, *Phys. Rev.* **D71** (2005) 054505, [[hep-lat/0406028](#)].
- [46] J. Bulava and S. Schaefer, *Improvement of $N_f = 3$ lattice QCD with Wilson fermions and tree-level improved gauge action*, *Nucl. Phys. B* **874** (2013) 188–197, [[arXiv:1304.7093](#)].
- [47] **ALPHA** Collaboration, A. Athenodorou, J. Finkenrath, F. Knechtli, T. Korzec, B. Leder, M. Krstić Marinković, and R. Sommer, *How perturbative are heavy sea quarks?*, *Nucl. Phys. B* **943** (2019) 114612, [[arXiv:1809.03383](#)].
- [48] M. Bruno, T. Korzec, and S. Schaefer, *Setting the scale for the CLS 2 + 1 flavor ensembles*, *Phys. Rev. D* **95** (2017), no. 7 074504, [[arXiv:1608.08900](#)].
- [49] S. Kurth, *The Renormalized quark mass in the Schrödinger functional of lattice QCD: A One loop calculation with a nonvanishing background field*. PhD thesis, Humboldt U., Berlin, 2002. [hep-lat/0211011](#).
- [50] **ALPHA** Collaboration, P. Fritzsche and T. Korzec, *Simulating the QCD Schrödinger Functional with three massless quark flavors, internal notes ALPHA Collaboration, in preparation for publication*.
- [51] M. T. Hansen and A. Patella, *Finite-volume effects in $(g - 2)_\mu^{HVP,LO}$* , *Phys. Rev. Lett.* **123** (2019) 172001, [[arXiv:1904.10010](#)].
- [52] G. M. de Divitiis, R. Petronzio, and N. Tantalo, *Distance preconditioning for lattice Dirac operators*, *Phys. Lett.* **B692** (2010) 157–160, [[arXiv:1006.4028](#)].
- [53] M. Lüscher and S. Schaefer, *Lattice QCD with open boundary conditions and twisted-mass reweighting*, *Comput. Phys. Commun.* **184** (2013) 519–528, [[arXiv:1206.2809](#)].
- [54] <http://luscher.web.cern.ch/luscher/openQCD/>.
- [55] M. Hasenbusch, *Speeding up the hybrid Monte Carlo algorithm for dynamical fermions*, *Phys. Lett. B* **519** (2001) 177–182, [[hep-lat/0107019](#)].
- [56] A. D. Kennedy, I. Horvath, and S. Sint, *A New exact method for dynamical fermion computations with nonlocal actions*, *Nucl. Phys. B Proc. Suppl.* **73** (1999) 834–836, [[hep-lat/9809092](#)].
- [57] M. A. Clark and A. D. Kennedy, *The RHMC algorithm for two flavors of dynamical staggered fermions*, *Nucl. Phys. B Proc. Suppl.* **129** (2004) 850–852, [[hep-lat/0309084](#)].
- [58] I. P. Omelyan, I. M. Mryglod, and R. Folk, *Symplectic analytically integrable decomposition algorithms: classification, derivation, and application to molecular dynamics, quantum and celestial mechanics simulations*, *Comp. Phys. Commun.* **151** (2003) 272.
- [59] I. S. Gradshteyn and I. M. Ryzhik, *Table of integrals, series, and products*. Elsevier/Academic Press, Amsterdam, seventh ed., 2007.